

Accelerating shape optimization by deep neural networks with on-the-fly determined architecture

Lucie Kubíčková^{a,c}, Ondřej Gebouský^{b,d}, Jan Haidl^{b,d}, Martin Isoz^{a,c,*}

^a *Institute of Thermomechanics of the Czech Academy of Sciences, Dolejškova 5, Prague 182 00, Czech Republic*

^b *Institute of Hydrodynamics of the Czech Academy of Sciences, Pod Patankou 5, Prague 166 12, Czech Republic*

^c *University of Chemistry and Technology, Prague, Department of Mathematics, Technická 5, Prague 166 28, Czech Republic*

^d *University of Chemistry and Technology, Prague, Department of Chemical Engineering, Technická 5, Prague 166 28, Czech Republic*

Abstract

In component shape optimization, the component properties are often evaluated by computationally expensive simulations. Such optimization becomes unfeasible when it is focused on a global search requiring thousands of simulations to be evaluated. Here, we present a viable global shape optimization methodology based on multi-objective evolutionary algorithms accelerated by deep neural networks (DNNs). Our methodology alternates between evaluating simulations and utilizing the generated data to train DNNs with various architectures. When a suitable DNN architecture is identified, the DNN replaces the simulation in the rest of the global search. Our methodology was tested on five ZDT benchmark functions, showing itself at the level of and sometimes more flexible than other state-of-the-art acceleration approaches. Then, it was applied to a real-life optimization problem, namely the shape optimization of a single-phase ejector. Compared with a non-accelerated methodology, ours was able to save weeks of CPU time in solving this problem. To experimentally confirm the performance of the optimized ejector shapes, four of them were 3D printed and tested on the lab scale confirming the predicted performance. This

*Corresponding author, tel: +420 26605 2832.

Email address: isozm@it.cas.cz (Martin Isoz)

URL: <https://www.it.cas.cz/en/d4/1041/> (Martin Isoz)

suggests that our methodology could be used for acceleration of other real-life shape optimization problems.

Keywords: multi-objective optimization, evolutionary algorithms, deep neural networks, computational fluid dynamics, ejector

1. Introduction

With ongoing technological advances, especially in 3D printing, device components of almost arbitrary shapes can be manufactured. Consequently, the design of the components can be tailored to a specific application, stimulating the development and utilization of various shape optimization methods. For components in contact with a fluid in motion, such as aircrafts, cars, or turbomachines, shape optimization methods are mostly backed by computational fluid dynamics (CFD) to evaluate component properties [1, 2]. However, CFD simulations of real-life problems are costly, limiting the viability of CFD-based shape optimization methods [3].

One viable option to shape optimization is to use gradient-based methods (GBMs), such as the sparse nonlinear optimizer [4] or the globally convergent method of moving asymptotes [5]. These GBMs are well recognized for their computational efficiency, even when handling hundreds of design variables [6]. When provided with a good enough starting point, they are well suited to find locally optimal solutions. However, they may struggle to find the global optimum [1].

Another optimization approach builds on stochastic (gradient-free) methods (SMs) that are usually divided into three groups, (i) particle swarm optimization [7], (ii) evolutionary algorithms [8, 9], and (iii) simulated annealing [10]. Contrary to the GBMs, none of these frameworks require continuity or predictability over the design space, and all of them are more resistant to getting trapped in a local optimum. However, as Yu et al. [11] shows for the case of wing shape optimization, SMs usually require by an order of magnitude more function evaluations than GBMs. Consequently, numerous attempts have been

made to combine SMs and GBMs to create hybrid methods that benefit from the strengths of both approaches, see, e.g., [12, 13, 14].

An alternative way to increase the viability of SMs is to pair them with computationally efficient surrogate models, creating the so-called surrogate-assisted optimization algorithms (SAOAs) [3]. The most widely used surrogate models are based on Gaussian process regression (aka Kriging models) [15, 16], radial basis functions [17, 18] or deep neural networks [19, 20]. However, the choice and construction of a suitable surrogate model is often problem-dependent and may require extensive testing prior to the optimization itself, limiting the method generality and flexibility.

In this work, we propose a surrogate-assisted optimization algorithm that utilizes multi-objective evolutionary algorithms (MOEAs) paired with deep neural networks (DNNs) where the main novelty is that the most suitable DNN architecture is found during the optimization run. Specifically, the methodology cycles between running an optimization with a CFD-based cost function and training of DNNs on intermediate optimization results. In each cycle, DNNs with different architectures are tested, and the features of the best DNN are passed on to the next cycle. When a sufficiently capable DNN is found, it replaces CFD in the optimization, and CFD is used further only for verification and corrective means.

Our methodology is first benchmarked using the ZDT functions proposed by Zitzler et al. [21] for testing multi-objective optimization algorithms. Its performance is compared with other similar state-of-the-art SAOAs [17, 22, 23]. Next, the methodology is used to solve a real-life optimization problem; namely, the shape optimization of a single-phase ejector. The motivation for this problem choice was twofold. First, it represents a relatively simple task for CFD simulations. Second, we have access to a specifically tailored experimental setup that was eventually used to validate the optimization results. Furthermore, the performance of the ejector is known to strongly depend on its geometry, and the effects of alterations in the geometry of its various parts on its performance have been investigated in recent decades [24, 25, 26]. In our case, the shape

optimization focused on the converging part and diffuser because these parts can be easily 3D printed and their optimized performance experimentally validated.

The paper proceeds as follows. First, multi-objective optimization is introduced in general, which is followed by a description of multi-objective evolutionary algorithms. Next, we provide details on our surrogate-assisted optimization algorithm. The algorithm is based on an adaptive connection between DNNs and CFD and is hereafter abbreviated as CFDNNetAdapt. In the subsequent part, the benchmarking using ZDT functions is introduced. Lastly, the real-life optimization problem is described in detail, and the optimization results are discussed. Details on the experimental setup and the used CFD model are given in the appendix.

2. Multi-objective shape optimization with CFD

2.1. Multi-objective optimization problem

Following the approach of Deb [27], a multi-objective optimization problem is defined as

$$\begin{aligned} & \min \mathbf{f}_{\text{cost}}(\mathbf{p}) \\ & \text{subject to } \mathbf{c} \leq 0 \text{ and } \mathbf{p}_{\min} \leq \mathbf{p} \leq \mathbf{p}_{\max} \end{aligned} \quad (1)$$

where $\mathbf{f}_{\text{cost}}(\mathbf{p}) = \mathbf{o}$ is a cost function, \mathbf{c} are considered constraints and \mathbf{p}_{\min} the minimum and \mathbf{p}_{\max} the maximum parameter bounds.

In case the objectives are anti-correlated, i.e., improving performance in one objective may worsen performance in the others, there does not exist a single optimal solution. Instead, a set of trade-off solutions is sought. This set is commonly referred to as the Pareto-optimal set (\mathcal{P}^*). Its counterpart with trade-off objective values is the Pareto-optimal front (\mathcal{O}^*) [28].

Trade-off solutions are identified as non-dominated solutions in terms of Pareto-dominance [28]. A non-dominated solution is defined as a solution that is not dominated by any other available solution. One solution (\mathbf{p}_1) dominates

another (\mathbf{p}_2) if

$$\begin{aligned} f_{\text{cost},i}(\mathbf{p}_1) &\leq f_{\text{cost},i}(\mathbf{p}_2) \text{ for all } i, i = 1, \dots, m \\ \text{and} \\ f_{\text{cost},i}(\mathbf{p}_1) &< f_{\text{cost},i}(\mathbf{p}_2) \text{ for at least one } i, i = 1, \dots, m \end{aligned} \tag{2}$$

where m is the number of objectives.

2.2. Multi-objective evolutionary algorithms

To solve a multi-objective optimization problem, we opted for using the multi-objective evolutionary algorithms (MOEAs) [9]. Of the many MOEA variants available, we used here the NSGA-II algorithm by Deb et al. [29]. The algorithm works with a population of individua that is updated each iteration. Each individuum is a tuple $(\mathbf{p}, \mathbf{f}_{\text{cost}}(\mathbf{p}))$. The population size (n_{pop}) is preset and the first population consists of individua with randomly generated vectors \mathbf{p} within a range defined by \mathbf{p}_{min} and \mathbf{p}_{max} .

In each iteration, random pairs of individua are chosen and mixed using partially random operators such as crossover and mutation, generating offspring individua with different \mathbf{p} vectors. The offspring individua are included in the population, and all the individua are sorted. In NSGA-II, the sorting is based on the Pareto-dominance principle. Lastly, the population size is reduced to n_{pop} by truncating the least fit individua identified by the sorting [29]. After this truncation, a new iteration starts. Note that each iteration is also referred to as a generation. The algorithm terminates after a preset number of generations (n_{gen}).

2.3. Baseline optimization framework

To have a baseline, a not-surrogate-assisted framework was prepared. The framework schematic is given in Figure 1. The core of the framework is implemented in Python. NSGA-II is included through an open-source Python library for multi-objective evolutionary optimization *Platypus* [30]. This library is combined with a custom code for the f_{cost} evaluation. For our real-life application,

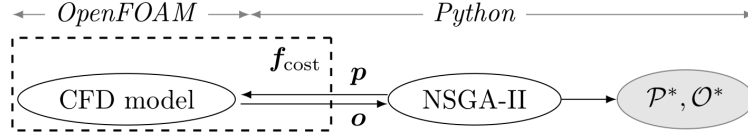


Figure 1: Schematic of the baseline optimization framework. Regions operated by either OpenFOAM or Python are distinguished. The vectors \mathbf{p} and \mathbf{o} contain the parameters and objectives, respectively. Furthermore, f_{cost} is the cost function, \mathcal{P}^* the Pareto-optimal set and \mathcal{O}^* the Pareto-optimal front.

the f_{cost} evaluation comprises an automated preparation of a CFD model in OpenFOAM [31]. The description of the CFD model construction for our real-life application (optimization of an ejector pump) is given in [Appendix B](#).

The framework is able to evaluate individua in each generation in parallel. In addition, the CFD models can also be evaluated in parallel. This allows for an effective run on high-performance computing architectures.

In this work, the baseline framework is used to generate (i) a referential solution (resulting \mathcal{P}^* , \mathcal{O}^*) for comparison with surrogate-assisted optimization algorithms, and (ii) data points (all evaluated tuples (\mathbf{p}, \mathbf{o})) for training of surrogate models.

3. Surrogate-assisted optimization

The bottleneck of CFD-driven optimizations is usually the long evaluation time of CFD simulations. Therefore, surrogate-assisted optimization algorithms (SAOAs) are often used to speed up the optimization. We prepared such a framework utilizing deep neural networks, namely multilayer perceptrons (MLPs).

Our proposed framework is similar to the adaptive evolution control frameworks as detailed in a review by Díaz-Manríquez et al. [3]. A novelty with respect to there-listed SAOAs lies in the fact that our framework (CFDNNetAdapt) includes an adaptive on-the-fly determination of a suitable MLP architecture. Note that even though our framework was designed for shape optimization having CFD as the expensive-to-evaluate cost function, it can be applied to any

optimization problem with real-valued cost function.

3.1. Multilayer perceptrons

A multilayer perceptron (MLP) is a feed-forward neural network that comprises several layers of neurons that are fully connected [32]. The first is the input layer, then there are several hidden layers, and the last is the output layer. In our framework, the MLP takes the parameters \mathbf{p} as input and provides a prediction of the objectives \mathbf{o} as the output. Therefore, the size of the first and last layer is equal to the number of parameters and objectives, respectively. The number of hidden layers is fixed (hyperparameter n_{hlrs}) and their size is optimized on-the-fly.

Regarding implementation, everything related to MLPs, e.g., construction or subsequent supervised learning, was implemented using an open-source Python library *pyrenn* [33].

3.2. CFDDNetAdapt

The schematic of CFDDNetAdapt is given in Figure 2. Its individual steps are described in detail in the following paragraphs. In addition, the hyperparameters of CFDDNetAdapt are summarized in Table 1.

Creation of MLPs. CFDDNetAdapt operates in iterations; in each iteration, a number of MLPs (hyperparameter n_{dnn}) is created. The transfer function used was always *tanh*. The number of hidden layers (hyperparameter n_{hlrs}) is the same for all MLPs, but the size of the hidden layers is varied. For the i -th hidden layer, its size is chosen randomly from an interval defined by an average value (\bar{n}_i) and half of its width (hyperparameter r_n), i.e.,

$$n_i = \min(n_{\text{max}}, \max(n_{\text{min}}, \tilde{n}_i)), \quad \tilde{n}_i = \text{random}(\bar{n}_i - r_n, \bar{n}_i + r_n), \quad (3)$$

where n_{max} and n_{min} are hyperparameters defining the maximal and minimal allowed layer size, respectively. Note that the interval half width is kept the same for all the hidden layers, but the average value can be different. In the first iteration, the averages are preset (hyperparameters \bar{n}_i^0 , $i = 1, \dots, n_{\text{hlrs}}$).

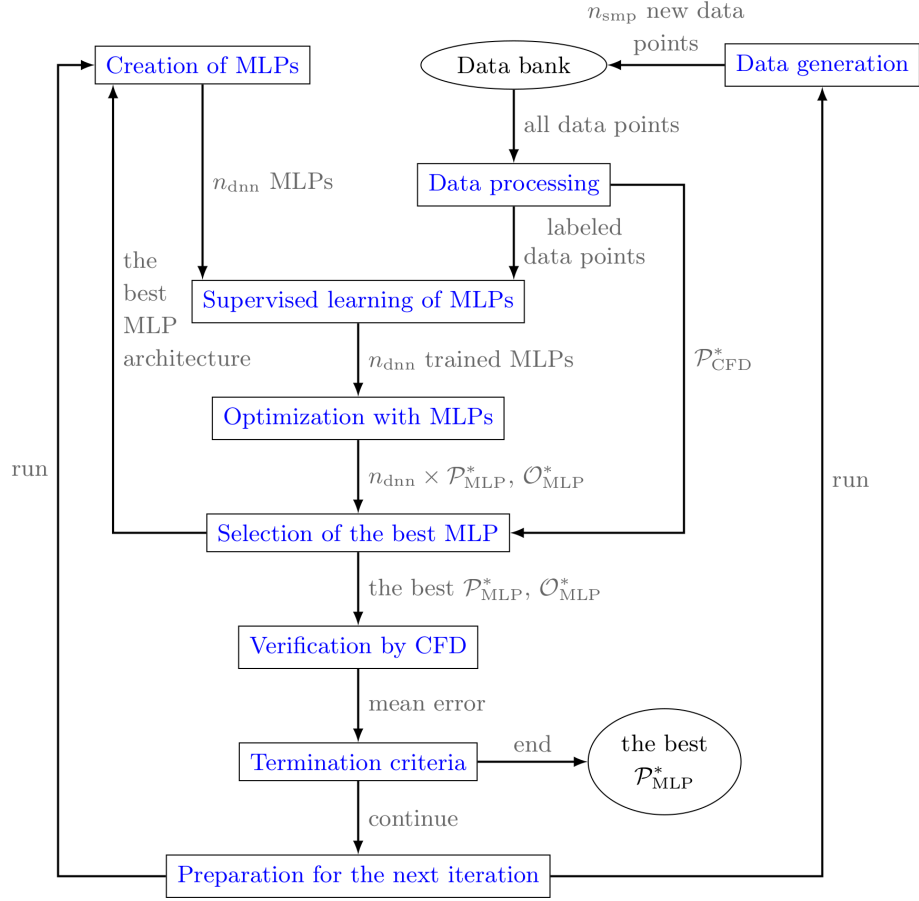


Figure 2: Schematics of steps and data-sharing in CFDNNNetAdapt. Used hyperparameters are listed in Table 1. MLP stands for "multilayer perceptron". Grey indicates passed data or signals.

hyperparameter	description	values used in Section 4 values used in Section 5
n_{hlrs}	number of hidden layers	3
		3
n_{dnn}	number of MLPs generated in each iteration	4
		10
r_n	half width of the interval for choosing hidden layer size	4
		4
n_{max}	maximal size of MLP layer	20
		20
n_{min}	minimal size of MLP layer	2
		2
\bar{n}_i^0	initial value for the average of the i -th hidden layer size	11 for any i
		11 for any i
n_{smp}	number of data points generated in one iteration	1000
		600
n_{pop}	population size for NSGA-II	100
		500
n_{gen}	number of generations for NSGA-II	250
		90
n_{ver}	number of points chosen for verification	16
		8
ϵ	required tolerance	10^{-4}
		0.05
k_{max}	maximum number of iterations	25
		12

Table 1: List of CFDDNetAdapt hyperparameters with description. The hyperparameters are ordered in the same way as they are mentioned in text.

In subsequent iterations, the averages are inherited from the best MLP found in the previous iteration.

Data generation. To perform a supervised learning of the created MLPs, data points (tuples (\mathbf{p}, \mathbf{o})) are required. A preset number of data points (hyperparameter n_{smp}) is generated by the baseline optimization framework described in Section 2.3 and saved in a data bank. If data points from previous iterations are present, the baseline framework is not started from scratch, but selects its initial population from the data bank.

Data processing. All data stored in the data bank are processed together. First, non-dominated points are identified and saved as an intermediate Pareto-optimal set, $\mathcal{P}_{\text{CFD}}^*$. Next, all data points are randomly divided into three groups for supervised learning of MLPs. Specifically, 75 % are labeled as training data, 15 % as validation data, and 10 % as testing data.

Supervised learning of MLPs. Each MLP is trained on the training data using the Levenberg-Marquardt algorithm [34, 35]. The validation data are used to track MLP performance during training, and if the performance worsens significantly, training is stopped to prevent overfitting [32]. After the training is completed, testing data are used to evaluate the performance of each MLP, and the results are saved to allow for during-run or after-run checks of the algorithm’s progress. Inclusion of the performance check based on the testing data is motivated by an effort to allow the user to identify the potential overfitting of adaptively selected MLP architectures to the validation data.

Optimization with MLPs. Each trained MLP is used as a surrogate in an optimization run by NSGA-II. Each optimization runs with a predefined population size (hyperparameter n_{pop}) and number of generations (hyperparameter n_{gen}). Hence, each MLP predicts its own Pareto-optimal set ($\mathcal{P}_{\text{MLP}}^*$) and front ($\mathcal{O}_{\text{MLP}}^*$).

Selection of the best MLP. The quality of each MLP-predicted Pareto-optimal set ($\mathcal{P}_{\text{MLP}}^*$) is estimated by comparing it with the intermediate Pareto-optimal

set identified from the data points ($\mathcal{P}_{\text{CFD}}^*$). The comparison is based on the evaluation of an inverted generational distance (IGD) defined as

$$\text{IGD}(\mathcal{P}_{\text{CFD}}^*, \mathcal{P}_{\text{MLP}}^*) = \frac{1}{\|\mathcal{P}_{\text{CFD}}^*\|} \sum_{\mathbf{x} \in \mathcal{P}_{\text{CFD}}^*} \min_{\mathbf{y} \in \mathcal{P}_{\text{MLP}}^*} \|\mathbf{x}, \mathbf{y}\|, \quad (4)$$

where the lower the IGD, the more similar the sets are. As the most suitable Pareto-optimal set, the one with the lowest IGD is chosen. This choice, which may be seen as method under-relaxation, originates from the decreasing reliability of sets with a higher IGD. When a poorly trained MLP is used in an optimization, it tends to exploit gaps in its training and come up with solutions that are far off from what it was trained on, thus potentially having a large prediction error. Therefore, the Pareto-optimal set with the lowest IGD is assumed to contain the lowest number of such exploited solutions.

The MLP-predicted Pareto-optimal set with the lowest IGD, the corresponding Pareto-optimal front, and the MLP that was used to create these are saved. The rest of the sets, fronts, and MLPs are discarded.

Verification by CFD. The suitability of the most promising MLP identified based on IGD is verified by CFD. A number (hyperparameter n_{ver}) of solutions is randomly chosen from the MLP-predicted Pareto-optimal set ($\mathcal{P}_{\text{MLP}}^*$). For each chosen solution, a corresponding CFD model is constructed and evaluated. It is possible that some of the chosen points cannot be evaluated by CFD, i.e., the computational mesh would be too non-orthogonal or skewed. In such cases, CFDNetAdapt randomly chooses substitute solutions from the set.

For the evaluated solutions, the predicted and re-evaluated objective values are compared, and the mean error is computed as

$$\delta := \frac{1}{n_{\text{ver}}} \sum_{i=1}^{n_{\text{ver}}} \|\mathbf{o}_{\text{MLP},i} - \mathbf{o}_{\text{CFD},i}\| \quad (5)$$

where \mathbf{o}_{MLP} and \mathbf{o}_{CFD} are vectors of predicted and true objectives, respectively.

Termination criteria. If the verification error is smaller than a predefined tolerance (ϵ), the CFDNetAdapt run is terminated. The most suitable Pareto-

optimal set ($\mathcal{P}_{\text{MLP}}^*$) and the currently best-performing MLP are returned. Another reason for termination is reaching a preset maximum number of iterations of CFDDNetAdapt (hyperparameter k_{max}).

Preparation for the next iteration. In the event that the algorithm did not end, the architecture of the most suitable MLP found in the current iteration is forwarded to the next iteration. In particular, the hidden layer sizes of the best MLP are used as the average sizes in the creation of new MLPs.

4. Benchmarking of CFDDNetAdapt

For the verification of CFDDNetAdapt, five benchmark optimization problems suggested by Zitzler et al. [21] were chosen. The problems are referred to as ZDT1, ZDT2, ZDT3, ZDT4, and ZDT6. All of these operate with real parameters and two objectives. The test function ZDT5 was not included as its parameters are decoded as bitstrings. The complete specification of the test functions chosen is given in Table 2. Optimal solutions to each problem are illustrated in black in Figure 3.

The performance of CFDDNetAdapt was compared with two widely used algorithms: (i) NSGA-II without any surrogate model [29], and (ii) state-of-the-art surrogate-assisted optimization algorithm SOCEMO [17]. In addition, a variant of CFDDNetAdapt with non-DNN surrogate model was constructed and tested to investigate the suitability of DNN usage. A more detailed description of each method settings is provided in the following paragraphs, and the results are depicted in Figures 3 and 4.

The solutions (Pareto-optimal fronts) found by NSGA-II are shown in Figure 3 in red. Similarly to Deb et al. [29], NSGA-II was run with population size $n_{\text{pop}} = 250$ and number of generations $n_{\text{gen}} = 100$. All evaluated data points (tuples (\mathbf{p}, \mathbf{o})) generated by NSGA-II ($\sim 25,000$) were used to feed the other SAOs.

CFDDNetAdapt solutions are depicted in blue. For each ZDT problem, two Pareto-optimal fronts corresponding to the same Pareto-optimal set are

name	parameters	cost functions	optimal sol.
ZDT1	$n = 10$	$f_1(\mathbf{p}) = p_1$	$p_1 \in [0, 1]$
	$p_i \in [0, 1]$	$f_2(\mathbf{p}) = g(\mathbf{p}) \left[1 - \sqrt{p_1/g(\mathbf{p})} \right]$	$p_i = 0$
	$i = 1, \dots, n$	$g(\mathbf{p}) = 1 + 9 \left(\sum_{i=2}^n p_i \right) / (n - 1)$	$i = 2, \dots, n$
ZDT2	$n = 10$	$f_1(\mathbf{p}) = p_1$	$p_1 \in [0, 1]$
	$p_i \in [0, 1]$	$f_2(\mathbf{p}) = g(\mathbf{p}) \left[1 - (p_1/g(\mathbf{p}))^2 \right]$	$p_i = 0$
	$i = 1, \dots, n$	$g(\mathbf{p}) = 1 + 9 \left(\sum_{i=2}^n p_i \right) / (n - 1)$	$i = 2, \dots, n$
ZDT3	$n = 10$	$f_1(\mathbf{p}) = p_1$	$p_1 \in [0, 1]$
	$p_i \in [0, 1]$	$f_2(\mathbf{p}) = g(\mathbf{p}) \left[1 - \sqrt{p_1/g(\mathbf{p})} - \frac{p_1}{g(\mathbf{p})} \sin(10\pi p_1) \right]$	$p_i = 0$
	$i = 1, \dots, n$	$g(\mathbf{p}) = 1 + 9 \left(\sum_{i=2}^n p_i \right) / (n - 1)$	$i = 2, \dots, n$
ZDT4	$n = 2$	$f_1(\mathbf{p}) = p_1$	$p_1 \in [0, 1]$
	$p_1 \in [0, 1]$	$f_2(\mathbf{p}) = g(\mathbf{p}) \left[1 - \sqrt{p_1/g(\mathbf{p})} \right]$	$p_i = 0$
	$p_2 \in [-5, 5]$	$g(\mathbf{p}) = 1 + 10(n - 1) + \sum_{i=2}^n [p_i^2 - 10 \cos(4\pi p_i)]$	$i = 2, \dots, n$
ZDT6	$n = 2$	$f_1(\mathbf{p}) = 1 - \exp(-4p_1) \sin^6(6\pi p_1)$	$p_1 \in [0, 1]$
	$p_i \in [0, 1]$	$f_2(\mathbf{p}) = g(\mathbf{p}) \left[1 - (f_1(\mathbf{p})/g(\mathbf{p}))^2 \right]$	$p_i = 0$
	$i = 1, \dots, n$	$g(\mathbf{p}) = 1 + 9 \left[\left(\sum_{i=2}^n p_i \right) / (n - 1) \right]^{0.25}$	$i = 2, \dots, n$

Table 2: Utilized ZDT functions [21].

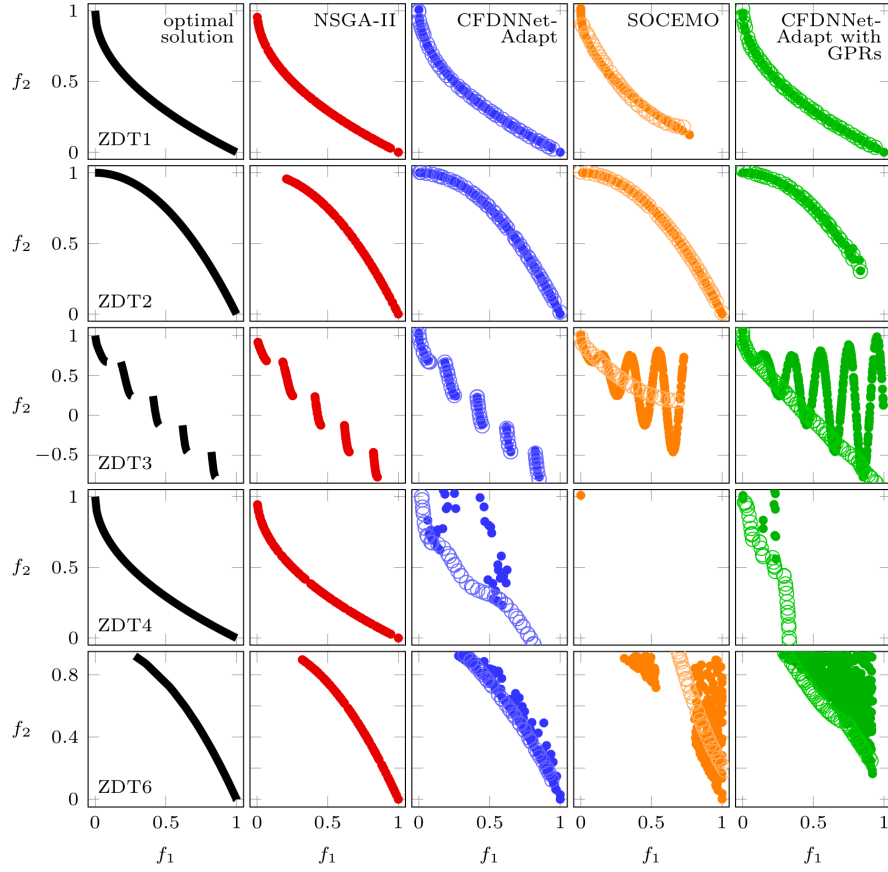


Figure 3: Comparison of solutions to the ZDT problems. From left to right, there are optimal solutions (black), solutions found by NSGA-II (red), solutions found by CFDNNNetAdapt (blue), solutions found by SOCEMO (orange), and solutions found by a CFDNNNetAdapt variant with GPRs (green). The empty circles depict the Pareto-optimal front as predicted by the surrogate model, the full circles show the corresponding true values.

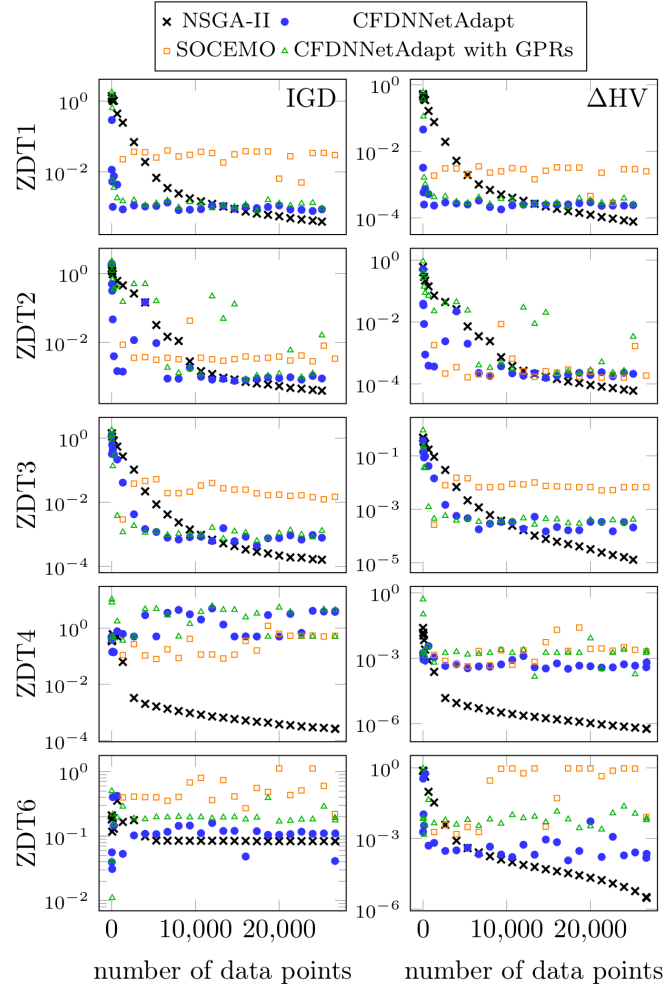


Figure 4: Evolution of the IGD (4) and ΔHV (6) indicators from NSGA-II, CFDDNetAdapt, CFDDNetAdapt variant with GPR and SOCEMO.

depicted: the one predicted by the best found surrogate model (empty circles) and its counter-part re-evaluated by the true cost functions (full circles). The results of the other SAOAs are depicted in the same way. Moreover, for all optimization problems, the same hyperparameter setting was used to keep the comparison fair; the setting is discussed in [Appendix C](#).

The solutions of SOCEMO [17] are shown in orange. The surrogates used by SOCEMO are based on radial basis functions (RBFs) and were originally used for problems with up to 500 data points. As we work with up to 25,000 points, we implemented a probabilistic selection of inducing points based on [36] to effectively lower the problem dimension.

Lastly, the solutions found by a variant of CFDNNetAdapt with non-DNN surrogate models are depicted in green. The surrogate models used were based on Gaussian process regression (GPR) [37]. The choice of GPR was motivated by its frequent use (mainly as Kriging models) in SAOAs, as described in, e.g. [22, 23].

Specifically, the sparse variant of the GPR with up to 50 inducing points was used. In each iteration, four GPR models with different kernels (squared exponential, Matern52, Matern32, and Matern12) were tested. The implementation was done using a Python library *gpflow* [38].

In addition to the comparison of Pareto-optimal fronts in Figure 3, the convergence of the mentioned algorithms was also examined. For each algorithm, the evolution of two indicators is depicted in Figure 4. The first indicator is the inverted generational distance defined in (4). Each resulting Pareto-optimal set \mathcal{P}^* was compared to the optimal set $\mathcal{P}_{\text{opt}}^*$, i.e., $\text{IGD}(\mathcal{P}_{\text{opt}}^*, \mathcal{P}^*)$ was computed.

The second indicator was based on the hyper-volume (HV) indicator. In two-dimensional objective space, HV represents an area that is non-dominated by points of a given Pareto-optimal front (\mathcal{O}^*) with respect to the preset reference point (\mathbf{r}). The formal definition of $\text{HV}(\mathcal{O}^*, \mathbf{r})$ is given in [39]. For our comparison, the scaled difference of HV to optimal HV (ΔHV) was examined.

It was computed as

$$\Delta\text{HV}(\mathcal{O}_{\text{opt}}^*, \mathcal{O}^*, \mathbf{r}) = \frac{\text{HV}(\mathcal{O}_{\text{opt}}^*, \mathbf{r}) - \text{HV}(\mathcal{O}^*, \mathbf{r})}{\text{HV}(\min(\mathcal{O}_{\text{opt}}^*), \mathbf{r})} \quad (6)$$

where $\mathcal{O}_{\text{opt}}^*$ comprises the optimal objective values. The reference point \mathbf{r} is problem dependent and was set as the maximal cost function values encountered by NSGA-II. Lastly, the term $\text{HV}(\min(\mathcal{O}_{\text{opt}}^*), \mathbf{r})$ represents the area of a rectangle defined by the minimal optimal values of the cost functions and the reference point.

For the problems ZDT1 and ZDT2, the SAOAs mostly converged to lower indicator values faster than NSGA-II. However, limitations are visible in Figure 3 for ZDT1-SOCOMO and ZDT2-GPRs where the algorithms were unable to uncover the whole Pareto-optimal front. This is also apparent in the convergence graphs in Figure 4, where in the respective cases the indicators jump by orders of magnitude even in the latter iterations. In one iteration, the surrogates are able to locate the whole front, in the subsequent they are not. In CFDNNetAdapt, the information about the best surrogate architectures is passed along iterations, which presumably helps to avoid this problem.

In ZDT3, the SAOAs still converged faster, but the problems were larger. Surrogate models based on GPRs and RBFs had considerable problems with the discontinuity of the Pareto-optimal front. CFDNNetAdapt with DNNs appears to be the most flexible. In ZDT4, all SAOAs failed. None of the surrogate models was able to give accurate enough predictions and most of the solutions predicted to lie on the Pareto-optimal front (empty circles in Figure 3) were actually far off the true values (full circles in Figure 3).

Lastly, in ZDT6, the inaccuracy of the predictions is also apparent. Nevertheless, the algorithms were able to locate the Pareto-optimal front. The least smudged front was provided by CFDNNetAdapt that also achieved the lowest indicator values. Moreover, the IGD indicator shows that even NSGA-II had problems identifying the whole Pareto-optimal set, the indicator stuck at about 10^{-1} .

Overall, CFDNNetAdapt works sufficiently well in comparison with other

available options. The usage of DNNs appears to be adequate when compared with models based on GPRs or RBFs. In addition, the flexibility of DNNs together with the CFDNNNetAdapt feature of passing architecture-relevant information to successive iterations gives the algorithm a slight advantage when dealing with non-continuous or complex optimization search spaces.

Still, the standardized tests performed suggest that, similarly to other SAOAs, the CFDNNNetAdapt algorithm is not universally usable. The main strength of CFDNNNetAdapt lies in accelerating optimizations with computationally intensive evaluation of cost functions. Based on examining Figures 3 and 4, a best-practice approach is proposed. First, CFDNNNetAdapt is the most advantageous for optimizations in topologically simple parameter and objective spaces (similar to ZDT1 and ZDT2). Second, for cases with complex objective space but simple parameter space (ZDT3), it can still provide satisfactory solutions with significantly fewer data points than NSGA-II. Third, for the cases of topologically complex parameter space (ZDT4 and ZDT6), the algorithm will fail. This failure is to be expected because in such cases, small variances in cost function parameters significantly affect the returned objectives, which makes construction of any data-driven surrogate problematic at best.

In cases where CFDNNNetAdapt can be applied, at least 250 data points should be available before initial training of the surrogate is attempted. Then, the algorithm usually provides the best trade-off between the quality of approximation of the Pareto-optimal solution to the original problem and the cost function evaluations for less than 2,500 data points. Using more than 2,500 data points is beneficial to ensure the CFDNNNetAdapt convergence. At 10,000 data points, CFDNNNetAdapt is usually outperformed by pure NSGA-II.

5. Real-life application

To illustrate the behavior of the CFDNNNetAdapt algorithm in a real-life application, we have selected the shape optimization of a single-phase ejector pump. Ejector pumps are technologically simple devices that utilize the kinetic

energy of a high-speed fluid jet to entrain a secondary fluid. Given their simple structure and absence of moving parts, ejectors are widely used, e.g., for the transport of fuel in aircraft wings [40], for the compression of coolant in refrigeration systems [41], etc. In addition to its relevance for process engineering, the focus on an ejector in this work was motivated by the fact that we have access to a specifically designed experimental setup, for details see [Appendix A](#). The availability of a highly modifiable experimental setup was leveraged to validate the performance of the optimized shapes.

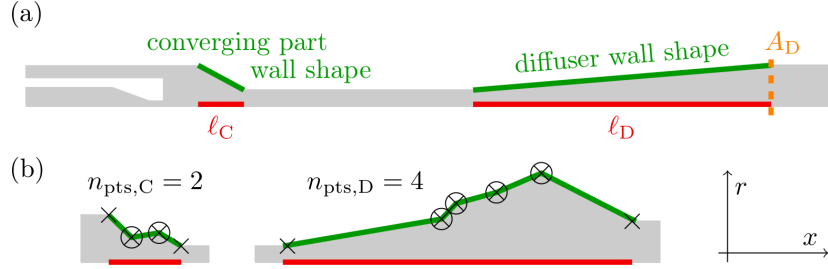


Figure 5: (a) Schematic of an ejector with the optimized parts highlighted in green and red. The plane A_D serves as a reference in the definition of ejector performance indicators. (b) Illustrative shapes of the converging part (left) and diffuser (right). The shapes are defined with fixed points (\times) and optimized control points (\otimes).

5.1. Shape parametrization

The optimization focused on the converging part and the diffuser of the ejector. The schematic of the ejector with the regions of interest highlighted is given in [Figure 5a](#).

The length and shape of the outer wall of the parts were optimized. The wall shape was designed as piecewise linear. This approach was selected in order to promote the final design robustness with respect to the boundary layer detachment, especially at the diffuser start. Examples of possible piecewise designs are in [Figure 5b](#).

Eventually, the design of the ejector was defined by two lengths (ℓ_C and ℓ_D) and coordinates of n_{pts} control points ($n_{\text{pts}} = n_{\text{pts},C} + n_{\text{pts},D}$) as indicated in

Figure 5b. Given the axisymmetric geometry of the ejector, each control point is defined by two coordinates, hence the total number of parameters in the optimization was $n_{\text{pars}} = 2n_{\text{pts}} + 2$. We chose to have $n_{\text{pts,C}} = 2$ control points that define the design of the converging part and $n_{\text{pts,D}} = 4$ control points for the diffuser. Consequently, the total number of parameters was $n_{\text{pars}} = 14$.

5.2. Constraints

Two design constraints were included. First, the total length of the experimental device is limited and therefore the sum of the lengths had to be kept below a predefined maximal value, i.e.

$$\ell_{\text{C}} + \ell_{\text{D}} \leq \ell_{\text{max}}. \quad (7)$$

Second, the control points must be sequentially ordered along the x axis. Having n_{pts} points, it must hold that

$$x_i > x_{i-1} \quad i = 2, \dots, n_{\text{pts}}. \quad (8)$$

The second constraint is crucial for effective automatic generation of meshes for CFD models.

5.3. Optimized objectives

The geometry of the ejector was optimized subject to two performance indicators: (i) the ejector energy efficiency (e_{eff}), and (ii) the total length (ℓ_{t}). The first indicator reflects the primary purpose of an ejector being used as a pump. Thus, its energy efficiency is of utmost interest and is defined as

$$e_{\text{eff}} = \frac{\bar{Q}_{\text{suction}}(\bar{p}_{\text{D}} - \bar{p}_{\text{suction}})}{\bar{Q}_{\text{inlet}}(\bar{p}_{\text{inlet}} - \bar{p}_{\text{D}})}, \quad \bar{\varphi}_A = \frac{1}{\|A\|} \int_A \varphi dS, \quad (9)$$

where \bar{Q} and \bar{p} are the surface-averaged volumetric flow rate and pressure, respectively. The subscripts in (9)₁ indicate the surfaces on which the averages are computed, i.e., *inlet*, *suction*, and the plane A_{D} as indicated in Figure 5a.

The energy efficiency was evaluated by CFD; particularly, using the OpenFOAM [31] library. Details about the generation of a CFD model, model

numerical settings, and validation are given in [Appendix B](#). For each ejector design, the CFD model was evaluated for three primary fluid flow rates ($\dot{Q}_{\text{inlet}} = \{0.3, 0.4, 0.5\} \text{ l/s}$) and an average value \bar{e}_{eff} was relevant for optimization.

In addition to e_{eff} , which is to be maximized, the second performance indicator, total length, reflects possible geometric constraints of the environment the ejector should be installed in; thus, it is to be minimized. The total length was defined as

$$\ell_t = \ell_C + \ell_D, \quad (10)$$

and according to our prior studies [\[42\]](#), minimization of ℓ_t is expected to be in anti-correlation with maximization of e_{eff} .

5.4. Penalization

In case the ejector geometry did not satisfy the design constraints [\(7\)](#) and [\(8\)](#), the performance indicators were not evaluated. Instead, a penalty was computed as

$$s_{\text{cons}} = 1.0 + \beta_\ell \cdot (\ell_C + \ell_D - \ell_{\text{max}}) + \beta_{\text{pts}} \cdot \sum_{\substack{i=2 \\ x_i < x_{i-1}}}^{n_{\text{pts}}} (x_{i-1} - x_i), \quad (11)$$

where β_ℓ and β_{pts} are constant weights that were set by trial and error as $\beta_\ell = 1.0$ and $\beta_{\text{pts}} = 10.0$.

Moreover, even though the design satisfied the constraints, it could happen that the generated CFD mesh was too skewed and non-orthogonal and, therefore, unsuitable for CFD calculation. In such cases, the values of skewness (γ_{skew}) and non-orthogonality ($\gamma_{\text{non-o}}$) indicators computed by OpenFOAM were used to compute a penalty as

$$s_{\text{mesh}} = 1.0 + \beta_s \cdot \gamma_{\text{skew}} + \beta_n \cdot \gamma_{\text{non-o}} \quad (12)$$

where β_{skew} and $\beta_{\text{non-o}}$ are weights that were estimated by trial and error as $\beta_{\text{skew}} = \beta_{\text{non-o}} = 0.1$.

5.5. Cost function

In summary, the cost function distinguished three cases. First, the constraints (7) and (8) were checked, and if either failed, the s_{cons} value was used. Second, the computational mesh was generated and its quality was estimated. When the quality of the mesh was insufficient, the value s_{mesh} was used. Third, the CFD model was calculated and the ejector performance indicators (9) and (10) were evaluated.

The cost function (\mathbf{f}_{cost}) can be written as

$$\mathbf{o} = \mathbf{f}_{\text{cost}}(\mathbf{p}) = \begin{cases} s_{\text{cons}}(\mathbf{p}) \cdot (1, 1)^T & \text{in first case} \\ s_{\text{mesh}}(\mathbf{p}) \cdot (1, 1)^T & \text{in second case} \\ (-\bar{e}_{\text{eff}}, \ell_t)^T & \text{in third case,} \end{cases} \quad (13)$$

where \mathbf{p} is the vector of parameters and \mathbf{o} the vector of objectives. Note that the cost function was minimized and therefore the energy efficiency was multiplied by -1 .

5.6. Generation of common data points for comparison

The described optimization problem was first pre-solved using the baseline framework described in Section 2.3. The reason for this is to create a common set of data points for a fair comparison of CFDNetAdapt with the baseline framework. In particular, (i) CFDNetAdapt will use the common data set as a source of data points instead of computing its own. (ii) The data points will be supplied to CFDNetAdapt in the same order as they were generated by the baseline framework to mimic the conditions when CFDNetAdapt creates its own data points. (iii) To compare CFDNetAdapt-aided optimization with the baseline framework, the baseline framework will be restarted, and the common data set will be used as a starting point.

To generate the common data points, the NSGA-II algorithm was run with population size $n_{\text{pop}} = 320$ and number of generations $n_{\text{gen}} = 30$. Overall, 9,600 ejector geometries were tested. However, approximately 25% of the tested geometries could not be evaluated by CFD, since they either violated the design

constraints or the computational mesh was too skewed and non-orthogonal, see Section 5.4. Therefore, the number of designs evaluated by CFD was about 7,200. Each design was evaluated for three primary fluid flow rates and the total number of evaluated CFD models was $3 \cdot 7,200 = 21,600$.

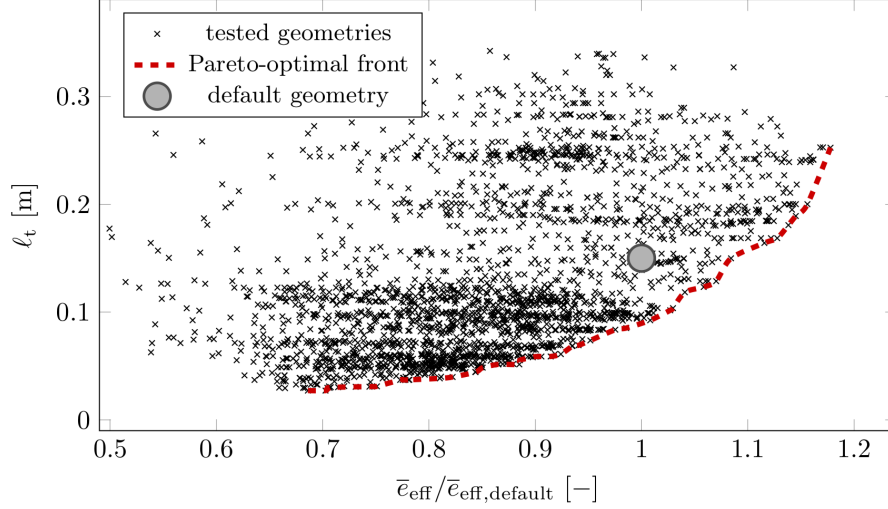


Figure 6: Results generated by the baseline framework in pre-solving of the optimization problem. Due to clarity, only a representative selection of the tested geometries, approximately a third of all the evaluated geometries, is depicted.

The common data points together with the Pareto-optimal front found by the baseline framework are depicted in Figure 6. For clarity of the graph, only a representative selection of all the ejector geometries is depicted. The selection was created such that no two ejector designs are too close to each other in the displayed objective space. In particular, when two points were closer than 10^{-2} in terms of Euclidean distance, one of them was omitted.

The illustrated data show that the Pareto-optimal front is not equally resolved in all parts of the objective space, especially in parts with $\ell_t > 0.1$ m and $\bar{e}_{\text{eff}}/\bar{e}_{\text{eff,default}} > 1.0$, the front is more sparse. Presumably, this is caused by the high dimensionality of the parameter space. Nonetheless, the Pareto-optimal front position did not change significantly in the last 5 generations of the NSGA-II run.

5.7. Comparison of CFDNNetAdapt and the baseline framework

The common data points were used to supply a run of CFDNNetAdapt with data and as a starting point for the continuation of the baseline framework. Ideally, CFDNNetAdapt should find new ejector designs that will (i) fill in the sparse regions of the pre-solved (common) Pareto-optimal front and (ii) be non-dominated by any of the already found solutions. This should be achieved at a fraction of the computational costs required to continue the baseline framework until it converges to similarly good results.

In each of its iterations, CFDNNetAdapt took $n_{\text{smp}} = 600$ points from the common data set. The points were taken in the same order as they were generated by the baseline framework. Regarding the CFDNNetAdapt hyperparameters, the total number of iterations was $k_{\text{max}} = 12$, $n_{\text{dnn}} = 10$ MLPs were created in each iteration, the number of hidden layers of each MLP was fixed to $n_{\text{hlrs}} = 3$ and each MLP was used as a surrogate in an optimization run by NSGA-II with $n_{\text{pop}} = 500$ and $n_{\text{gen}} = 90$. More details about the hyperparameters are given in [Appendix C](#).

It took CFDNNetAdapt 10 iterations (6,600 samples) to achieve verification error $\delta = 0.036$, see (5), and to meet the required tolerance $\epsilon = 0.05 \approx 5\%$ average error in the optimized objectives. The best MLP found had 5 fully connected layers with 14, 5, 12, 12 and 2 neurons. In Figure 7a, a representative selection of solutions is shown. The selection comprises about 500 solutions chosen not only from the resulting Pareto-optimal set $\mathcal{P}_{\text{MLP}}^*$ but also from the last 10 generations of NSGA-II with the best MLP used as a surrogate. Each of the solutions shown was re-evaluated by CFD.

For the continuation of the baseline framework, the common data set was used as a starting point. To achieve results comparable to those shown in Figure 7a, the NSGA-II algorithm had to be continued for $n_{\text{gen}} = 30$ generations evaluating additional 9,600 ejector designs. The results of the continuation are depicted in Figure 7b. Similarly to Figure 7a, the representative selection shown comprises about 500 solutions chosen from the $\mathcal{P}_{\text{CFD}}^*$ and the last 10 generations of the continuation of NSGA-II.

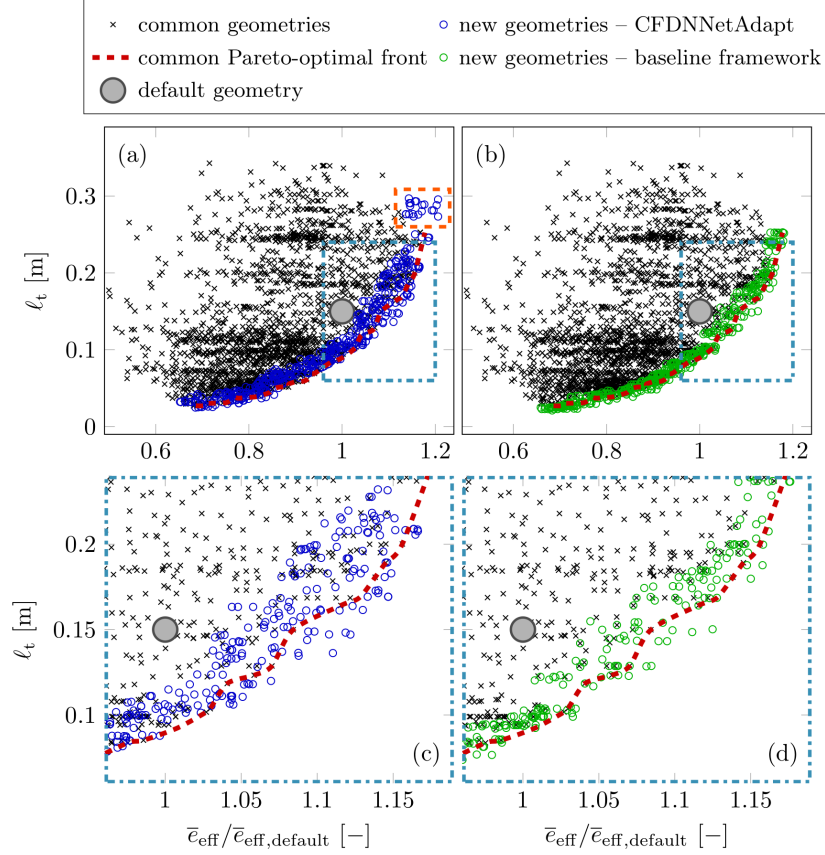


Figure 7: Common data points from Figure 6 displayed with new ejector geometries. (a) New geometries were found by CFDNNetAdapt with the values of \bar{e}_{eff} recomputed by CFD. (b) New geometries found by continuation of the baseline framework. (c) and (d) Zoom on the data in dash-dotted teal boxes in (a) and (b), respectively. Geometries found by CFDNNetAdapt only are highlighted by a dashed orange box.

Comparing the results depicted in Figures 7c and d, it may be concluded that with respect to filling the gaps in the pre-solved (common) Pareto-optimal front, CFDNetAdapt slightly outperforms the continuation of the baseline framework. More importantly, CFDNetAdapt was able to find geometries further expanding the common Pareto-optimal front while the baseline framework did not find similar designs, see the dashed orange box in Figure 7a. On the other hand, the new designs found by CFDNetAdapt dominated only 55 % of the pre-solved (common) non-dominated designs. The continuation of the baseline framework was able to dominate 85 %.

Regarding the computational resources used, the continuation of the baseline framework took about 6,912 core-hours on AMD EPYC™ 7552 2nd Gen. On the other hand, CFDNetAdapt took about 152 core-hours to find a good MLP architecture and use it as a surrogate in an optimization. The subsequent re-evaluation of the 500 ejector designs shown in Figure 7a took about 480 core-hours.

5.8. Validation of selected designs

To support the results presented in Figures 6 and 7, the performance of two designs found by the CFD-driven framework and two found by CFDNetAdapt was subjected to experimental validation. The designs that were chosen are depicted in Figure 8 in blue and green (baseline framework) and orange and red (CFDNetAdapt).

To complement the measurements, two more ejector designs were added to the validation plans, (i) the default ejector design (depicted in gray) (ii) and design with same component lengths as the green one but non-altered wall shapes (depicted in black). The six geometries were 3D-printed and prepared for experimental testing using the manufacturing process described in Appendix A.

With each design, measurements were made for several different primary fluid flow rates \dot{Q}_{inlet} . In addition, a corresponding CFD model was constructed for each measured data point. The complete results of the validation are presented in Appendix D.

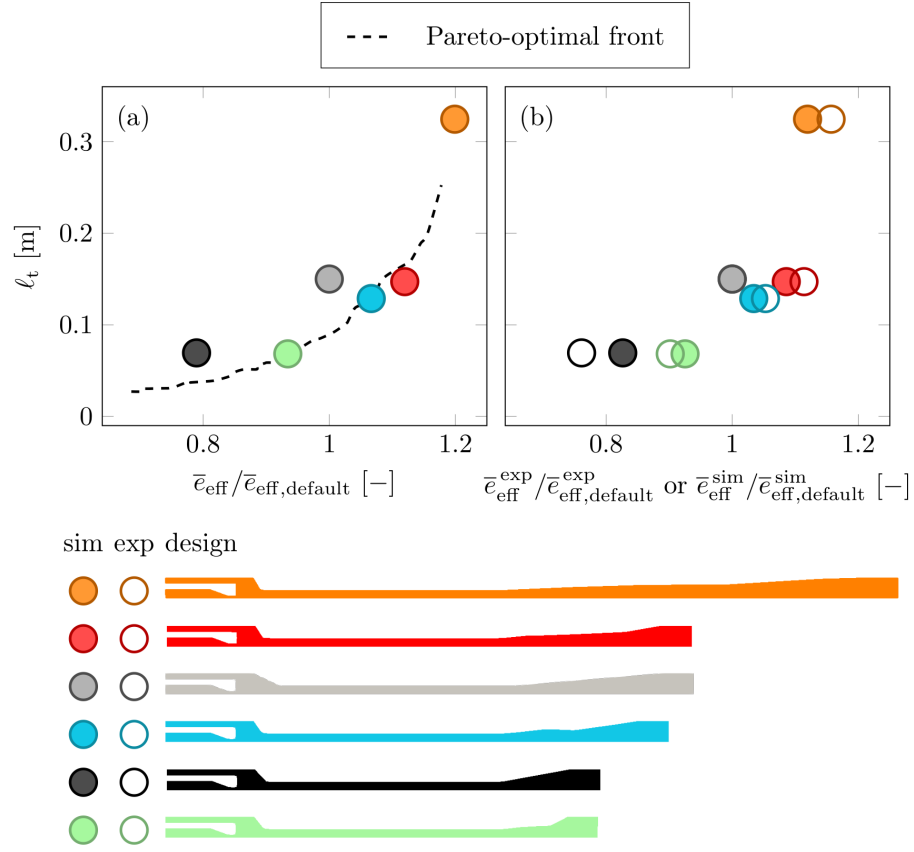


Figure 8: (a) The Pareto-optimal front depicted in Figure 6 with highlighted designs that were subject to experimental validation. (b) Performance of designs highlighted in (a) calculated from experimental data and corresponding CFD models.

The data from the measurements performed with the primary fluid flow rates closest to those used in optimization ($\dot{Q}_{\text{inlet}} = \{0.3, 0.4, 0.5\}$ l/s) were then used to calculate the average energy efficiency \bar{e}_{eff} by (9). For each design, the efficiency obtained from optimization is given in Figure 8a and the efficiency calculated from experimental data ($\bar{e}_{\text{eff}}^{\text{exp}}$) and the corresponding CFD model ($\bar{e}_{\text{eff}}^{\text{sim}}$) in Figure 8b.

The agreement with the experimental data is not perfect, which can be attributed to the simplistic and optimization-oriented approach to CFD. Nevertheless, the trends in performance predicted by optimization hold in the experiment as well.

6. Summary and conclusion

In this paper, we presented CFDNNAdapt, an adaptive optimization methodology that integrates computational fluid dynamics (CFD) with multi-objective evolutionary algorithms (MOEA) and is accelerated by deep neural networks (DNNs). The methodology represents a surrogate-assisted approach to reducing computational time and enhancing the efficiency of CFD-based multi-objective optimization. CFDNNAdapt was tested on several ZDT benchmark functions and applied to a real-life problem of shape optimization of a single-phase ejector, the results of which were validated using experimental data.

The tests on ZDT functions showed that CFDNNAdapt is at the level of or outperforming similar state-of-the-art methods as SOCEMO [17], or algorithms based on Gaussian process regression [22, 23]. Furthermore, it was listed that for sufficiently simple optimization parameter and objective space, CFDNNAdapt should be initialized with at least 250 data points available, but it can be expected to provide a better accuracy-to-cost ratio than NSGA-II for up to 10,000 data points.

The application of CFDNNAdapt to the shape optimization of an ejector further demonstrated its efficiency. This optimization represented a 14-parameter constrained problem in which the cost function was evaluated us-

ing either CFD or problem-specific penalty functions. Compared with a non-accelerated approach, CFDNNetAdapt found a wider variety of optimal ejector designs requiring a fraction of CPU time.

Future work will aim to address weak points of the approach, such as the dependency of CFDNNetAdapt on hyperparameter tuning. Additionally, the scalability of CFDNNetAdapt to other more complex real-life geometries was not fully investigated. For complex geometries, it is favorable to utilize CFD models based on an immersed boundary method for easier geometry change. However, CFDNNetAdapt in its present form is not prepared for that.

CFDNNetAdapt is an open-source project. Its source code and the simulation source codes and settings required to reproduce all the computations of this study are available from <https://github.com/techMathGroup/CFDNNetAdapt>.

Acknowledgments

This research was co-funded by the European Union under the project Metamaterials for thermally stressed machine components (reg. no. CZ.02.01.01/00/23_020/0008501). The work was financially supported by the institutional support RVO:61388998 and RVO:67985874, and the grant project with No. QL24010110 of the National Agency for Agricultural Research (NAAR). Finally, this work was supported from the grant of Specific university research – A1_FCHI_2025_004 and A1_FCHI_2025_002.

Nomenclature

A	plane, $[-]$
\mathbf{c}	constraints, $[-]$
d	diameter, $[L]$
e_{eff}	energy efficiency, $[-]$
\mathbf{f}_{cost}	cost function, $[-]$
\mathbf{g}	gravitational acceleration, $[L\ T^{-2}]$
I	turbulence intensity, $[-]$
k	turbulence kinetic energy, $[L^2\ T^{-2}]$
k_{max}	maximum number of iterations, $[-]$
K_{arm}	pipng resistance, $[L^{-4}]$
ℓ	length, $[L]$
m	number of objectives, $[-]$
n_{dnn}	number of deep neural networks, $[-]$
n_{gen}	number of generations, $[-]$
n_{hlrs}	number of hidden layers, $[-]$
n_{pars}	number of parameters, $[-]$
n_{pop}	population size, $[-]$
n_{pts}	number of points, $[-]$
n_{smp}	number of samples, $[-]$
n_{ver}	number of verification cases, $[-]$
\mathbf{n}	outer unit normal, $[-]$
\bar{n}	average size of a hidden layer, $[-]$
\mathbf{o}	objectives, $[-]$
\mathcal{O}^*	Pareto-optimal front, $[-]$
p	pressure, $[M\ L^{-1}\ T^{-2}]$
\bar{p}	kinematic pressure, $[L^2\ T^{-2}]$
\mathbf{p}	parameters, $[-]$
\mathcal{P}^*	Pareto-optimal set, $[-]$
\dot{Q}	volumetric flow rate, $[L^3\ T^{-1}]$
\mathbf{r}	reference point, $[-]$
r_{area}	ratio of suction area in experiment and in simulation, $[-]$
r_n	half width of an interval of hidden layer size, $[-]$
r_Q	secondary-to-primary flow rate ratio, $[-]$
Re	Reynolds number, $[-]$
s_{cons}	penalty from geometry constraints, $[-]$
s_{mesh}	penalty from mesh constraints, $[-]$
\mathbf{u}	velocity, $[L\ T^{-1}]$
\mathbf{x}	coordinates, $[L]$

Greek letters

β	penalty function coefficient, $[-]$
γ	mesh quality indicator, $[-]$
δ	mean error, $[-]$
$\Delta_s p$	scaled device pressure drop, $[-]$
ϵ	tolerance, $[-]$
ε	dissipation of turbulence kinetic energy, $[\text{L}^2 \text{T}^{-3}]$
ν	kinematic viscosity, $[\text{L}^2 \text{T}^{-1}]$
$\boldsymbol{\tau}$	viscous stress tensor, $[\text{L}^2 \text{T}^{-2}]$
$\boldsymbol{\tau}'$	Reynolds stress tensor, $[\text{L}^2 \text{T}^{-2}]$
ω	specific dissipation of turbulence kinetic energy, $[\text{T}^{-1}]$
Ω	computational domain, $[-]$

Subscripts and superscripts

B	nozzle body
C	converging part
D	diffuser
exp	experiment
G	gap part
M	mixing tube
min	minimum
max	maximum
N	nozzle
non-o	non-orthogonality
opt	optimal
s	scaled
sim	simulation
skew	skewness
smp	samples
t	total

Abbreviations

CFD	computational fluid dynamics
CFDNNetAdapt	optimization algorithm proposed in this work
CPU	central processing unit
DNN	deep neural network
GBM	gradient-based method
GPR	gaussian process regression
HV	hyper-volume
IGD	inverted generational distance
MLP	multi-layer perceptron
MOEA	multi-objective evolutionary algorithm
MOP	multi-objective optimization problem
NSGA-II	non-dominated sorting genetic algorithm II
RBF	radial basis function
SAOA	surrogate-assisted optimization algorithm
SOCEMO	algorithm for surrogate optimization of computationally expensive multiobjective problems
SM	stochastic method
ZDT	Zitzler-Dep-Thiele test function

References

- [1] S. Skinner, H. Zare-Behtash, State-of-the-art in aerodynamic shape optimisation methods, *Applied Soft Computing* 62 (2018) 933–962.
- [2] Z. Li, X. Zheng, Review of design optimization methods for turbomachinery aerodynamics, *Progress in Aerospace Sciences* 93 (2017) 1–23.
- [3] A. Díaz-Manríquez, G. Toscano, J. Barron-Zambrano, E. Tello-Leal, A review of surrogate assisted multiobjective evolutionary algorithms, *Computational Intelligence and Neuroscience* 2016 (2016) 9420460.
- [4] P. Gill, W. Murray, M. Saunders, SNOPT: an SQP algorithm for large-scale constrained optimization, *SIAM Review* 47 (2005) 99–131.

- [5] K. Svanberg, The method of moving asymptotes – a new method for structural optimization, *International Journal for Numerical Methods in Engineering* 24 (1987) 359–373.
- [6] N. Foster, G. Dulikravich, Three-dimensional aerodynamic shape optimization using genetic and gradient search algorithms, *Journal of Spacecraft and Rockets* 34 (1997) 36–42.
- [7] R. Eberhart, J. Kennedy, A new optimizer using particle swarm theory, in: *MHS’95. Proceedings of the Sixth International Symposium on Micro Machine and Human Science*, 1995, pp. 39–43. doi:[10.1109/MHS.1995.494215](https://doi.org/10.1109/MHS.1995.494215).
- [8] D. Goldberg, *Genetic Algorithms in Search, Optimization, and Machine Learning*, Addison-Wesley publishing company, inc., 1989.
- [9] M. Emmerich, A. Deutz, A tutorial on Multiobjective Optimization: Fundamentals and Evolutionary Methods, *Natural Computing* 17 (2018) 585–609.
- [10] S. Kirkpatrick, C. Gelatt, M. Vecchi, Optimization by simulated annealing, *Science* 220 (1983) 671–680.
- [11] Y. Yu, Z. Lyu, Z. Xu, J. Martins, On the influence of optimization algorithm and initial design on wing aerodynamic shape optimization, *Aerospace Science and Technology* 75 (2018) 183–199.
- [12] P. Gage, I. Kroo, I. Sobieski, Variable-complexity genetic algorithm for topological design, *AIAA Journal* 33 (1995) 2212–2217.
- [13] A. Vicini, D. Quagliarella, Airfoil and wing design through hybrid optimization strategies, *AIAA Journal* 37 (1999) 634–641.
- [14] J.-H. Kim, B. Ovgor, K.-H. Cha, J.-H. Kim, S. Lee, K.-Y. Kim, Optimization of the aerodynamic and aeroacoustic performance of an axial-flow fan, *AIAA Journal* 52 (2014) 2032–2044.

- [15] T. Chugh, Y. Jin, K. Miettinen, J. Hakanen, K. Sindhya, A surrogate-assisted reference vector guided evolutionary algorithm for computationally expensive many-objective optimization, *IEEE Transactions on Evolutionary Computation* 22 (2018) 129–142.
- [16] J. Knowles, ParEGO: A hybrid algorithm with on-line landscape approximation for expensive multiobjective optimization problems, *IEEE Transactions on Evolutionary Computation* 10 (2006) 50–66.
- [17] J. Müller, SOCEMO: Surrogate optimization of computationally expensive multiobjective problems, *INFORMS J. Comput.* 29 (2017) 581–596.
- [18] H. Dong, J. Li, P. Wang, B. Song, X. Yu, Surrogate-guided multi-objective optimization (sgmoo) using an efficient online sampling strategy, *Knowledge-Based Systems* 220 (2021) 106919.
- [19] Y. Tian, J. Hu, C. He, H. Ma, L. Zhang, X. Zhang, A pairwise comparison based surrogate-assisted evolutionary algorithm for expensive multi-objective optimization, *Swarm and Evolutionary Computation* 80 (2023) 101323.
- [20] A. Wolday, M. Ramteke, Surrogate model-based optimization of methanol synthesis process for multiple objectives: A pathway towards achieving sustainable development goals, *Chemical Engineering Research and Design* 204 (2024) 172–182.
- [21] E. Zitzler, K. Deb, L. Thiele, Comparison of multiobjective evolutionary algorithms: Empirical results, *Evolutionary Computation* 8 (2000) 173–195.
- [22] Y. Morita, S. Rezaeiravesh, N. Tabatabaei, R. Vinuesa, K. Fukagata, P. Schlatter, Applying bayesian optimization with gaussian process regression to computational fluid dynamics problems, *Journal of Computational Physics* 449 (2022) 110788.

- [23] F. Mastrippolito, S. Aubert, F. Ducros, Kriging metamodels-based multi-objective shape optimization applied to a multi-scale heat exchanger, *Computers & Fluids* 221 (2021) 104899.
- [24] P. Havelka, V. Linek, J. Sinkule, J. Zahradnik, M. Fialova, Effect of the ejector configuration on the gas suction rate and gas hold-up in ejector loop reactors, *Chemical Engineering Science* 52 (1997) 1701–1713.
- [25] T. Utomo, Z. Jin, M. Rahman, H. Jeong, H. Chung, Investigation on hydrodynamics and mass transfer characteristics of a gas-liquid ejector using three-dimensional CFD modeling, *Journal of Mechanical Science and Technology* 22 (2009) 1821–1829.
- [26] S. Daniels, A. Rahat, G. Tabor, J. Fieldsend, R. Everson, Automated shape optimization of a plane asymmetric diffuser using combined Computational Fluid Dynamic simulations and multi-objective Bayesian methodology, *International Journal of Computational Fluid Dynamics* 33 (2019) 256–271.
- [27] K. Deb, *Multi-objective Optimization Using Evolutionary Algorithms*, Wiley, 2001.
- [28] V. Pareto, *Course d’Economie Politique*, Librairie Droz, 1896.
- [29] K. Deb, A. Pratap, S. Agarwal, T. Meyarivan, A fast and elitist multiobjective genetic algorithm: NSGA-II, *IEEE Transactions on Evolutionary Computation* 6 (2002) 182–197.
- [30] D. Hadka, Platypus, A Free and Open Source Python Library for Multiobjective Optimization, 2020. URL: <https://github.com/Project-Platypus/Platypus>.
- [31] OpenCFD, OpenFOAM: The Open Source CFD Toolbox. User Guide Version 1.4, OpenCFD Limited, Reading UK, 2007.
- [32] I. Goodfellow, Y. Bengio, A. Courville, *Deep Learning*, MIT Press, 2016.

- [33] D. Atabay, Institute for Energy Economy and Application Technology, Technische Universität München, pyrenn: A recurrent neural network toolbox for python and matlab, 2018. URL: <https://pyrenn.readthedocs.io/en/latest/>.
- [34] K. Levenberg, A method for the solution of certain problems in least squares, *Quarterly of Applied Mathematics* 2 (1944) 164–168.
- [35] D. Marquardt, An algorithm for least-squares estimation of nonlinear parameters, *Journal of the Society for Industrial and Applied Mathematics* 11 (1963) 431–441.
- [36] A. Uhrenholt, V. Charvet, B. Jensen, Probabilistic selection of inducing points in sparse gaussian processes, in: *Proceedings of the Thirty-Seventh Conference on Uncertainty in Artificial Intelligence (UAI 2021)*, 2021, pp. 1035–1044. doi:[10.48550/arXiv.2010.09370](https://doi.org/10.48550/arXiv.2010.09370).
- [37] D. Jones, M. Schonlau, W. Welch, Efficient global optimization of expensive black-box functions, *Journal of Global Optimization* 13 (1998) 455–492.
- [38] A. de G. Matthews, M. van der Wilk, T. Nickson, K. Fujii, A. Boukouvalas, P. León-Villagrà, Z. Ghahramani, J. Hensman, GPflow: A Gaussian process library using TensorFlow, *Journal of Machine Learning Research* 18 (2017) 1–6.
- [39] A. Guerreiro, C. Fonseca, L. Paquete, The hypervolume indicator: Computational problems and algorithms, *ACM computing surveys* 54 (2021) 42.
- [40] M. Marini, A. Massardo, A. Satta, M. Geraci, Low area ratio aircraft fuel jet pump performances with and without cavitation, *Journal of Fluids Engineering* 114 (1992) 626–631.
- [41] S. Taleghani, M. Sorin, S. Poncet, Modeling of two-phase transcritical CO₂ ejectors for on-design and off-design conditions, *International Journal of Refrigeration* 87 (2018) 91–105.

- [42] L. Kubíčková, M. Isoz, J. Haidl, Increasing ejector efficiency via diffuser shape optimization, in: D. Šimurda, T. Bodnár (Eds.), *Proceedings of Topical Problems of Fluid Mechanics 2021*, IT CAS, 2021, pp. 79–86. doi:[10.14311/TPFM.2021.011](https://doi.org/10.14311/TPFM.2021.011).
- [43] O. Gebouský, K. Mařík, J. Haidl, M. Zedníková, Enhancement of gas entrainment rate in liquid-gas ejector pump, *Chemical Engineering Research and Design* 189 (2023) 117–125.
- [44] B. Launder, D. Spalding, The numerical computation of turbulent flows, *Computer Methods in Applied Mechanics and Engineering* 3 (1974) 269–289.
- [45] S. E. Tahry, k - ϵ equation for compressible reciprocating engine flows, *Journal of Energy* 7 (1983) 345–353.
- [46] T. Shih, W. Liou, A. Shabbir, Z. Yang, J. Zhu, A new k - ϵ eddy viscosity model for high Reynolds number turbulent flows, *Computers & Fluids* 24 (1995) 227–238.
- [47] D. Wilcox, *Turbulence modeling for CFD*, 3 ed., DCW Industries, USA, 2006.
- [48] F. Menter, Improved two equation k - ω turbulence models for aerodynamic flows, Technical Report N93-22809, NASA, 1992.
- [49] A. Hellsten, Some improvements in Menter’s k - ω SST turbulence model, in: *Proceedings of the Fluid Dynamics Conference*, volume 71, AIAA, 1997, pp. 1–11. doi:[10.2514/6.1998-2554](https://doi.org/10.2514/6.1998-2554).
- [50] F. Russo, N. Basse, Scaling of turbulence intensity for low-speed flow in smooth pipes, *Flow Measurement and Instrumentation* 52 (2016) 101–114.
- [51] S. Patankar, D. Spalding, A calculation procedure for heat, mass and momentum transfer in three-dimensional parabolic flows, *International Journal of Heat and Mass Transfer* 15 (1972) 1787–1806.

- [52] F. Moukalled, M. Darwish, L. Mangani, The finite volume method in computational fluid dynamics: an advanced introduction with OpenFOAM and Matlab, 1 ed., Springer-Verlag, Berlin, Germany, 2016.
- [53] P. Roe, Characteristics-based schemes for the Euler equations, Annual Reviews of Fluid Mechanics 18 (1986) 337–365.

Appendix A. Experimental set-up and default geometry

Measurements were performed on a modular laboratory-scale ejector unit, allowing liquid-liquid and liquid-gas process variants to be used. In the present study, water at ambient temperature was used as both the primary fluid (driving) and the secondary fluid (entrained), that is, the ejector was operated in the liquid-liquid regime.

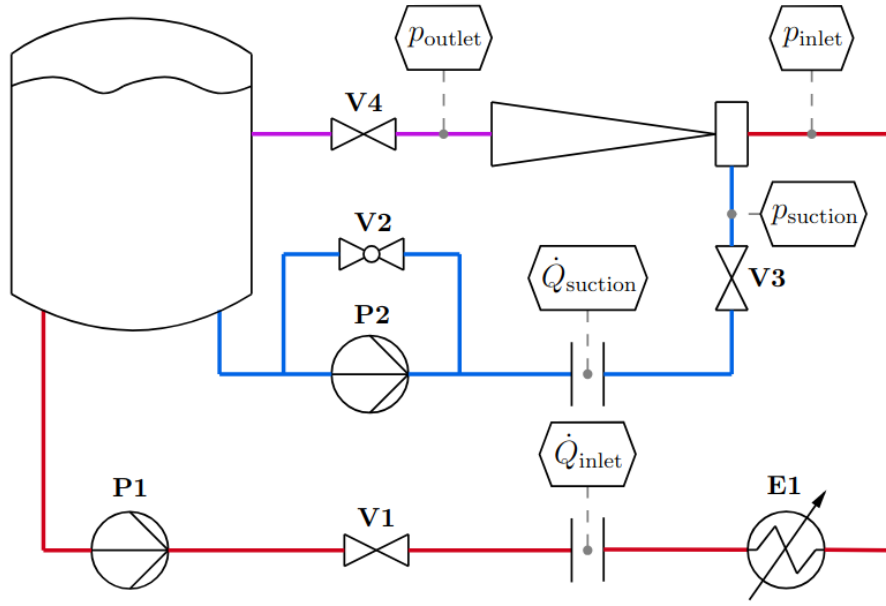


Figure A.1: Sketch of the experimental setup. P1,P2 - centrifugal pumps; E1 - heat exchanger; V1-V4 - valves; red lines - primary (driving) fluid; blue lines - secondary (entrained) fluid; magenta lines - mixed stream.

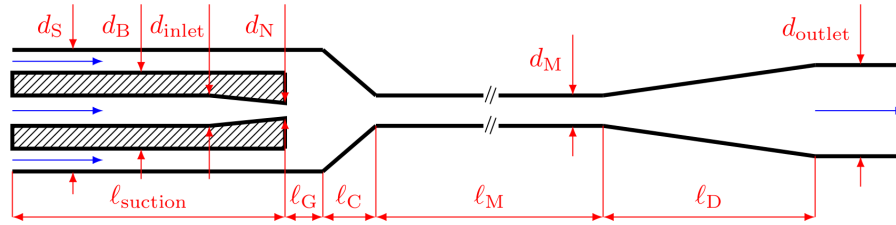


Figure A.2: Annotated drawing of the default ejector geometry.

dim.	value [mm]	dim.	value [mm]	dim.	value [mm]
d_{suction}	35	d_{B}	25	d_{inlet}	16
d_{N}	{4.3, 5.0, 7.0}	d_{M}	{14, 19}	d_{outlet}	35.6
ℓ_{suction}	60	ℓ_{G}	15	ℓ_{C}	20
ℓ_{M}	200	ℓ_{D}	130	—	—

Table A.1: Default values of ejector dimensions depicted in Figure A.2.

The experimental setup is sketched in Figure A.1. The setup comprises a 60 L storage tank from which water is pumped using the centrifugal pump P1 through the control valve V1, a heat exchanger E1, and a nozzle to the suction chamber of the ejector unit sketched in Figure A.2 with dimensions given in Table A.1. To allow independent pressure control in the suction chamber p_{suction} , the secondary fluid is delivered using a second centrifugal pump P2; the pressure in the suction chamber is adjusted by the throttling valve V3. Similarly, the pressure difference between the suction chamber and the diffuser outlet is controlled by the throttling valve V4.

Primary (\dot{Q}_{inlet}) and secondary fluid flow rates (\dot{Q}_{suction}) were measured as the pressure difference of the calibrated orifices; the relative uncertainty of the flow rate is less than 1% of the reading. The pressure in front of the nozzle (p_{inlet}) was measured using the Cressto SR transducer calibrated for the relative pressure range from -100 kPa to 1000 kPa with the uncertainty of ± 5 kPa; for the measurement of the pressures in the suction chamber (p_{suction}) and at the diffuser outlet (p_{outlet}), the Cressto SR transducers were calibrated for the relative pressure range from -100 kPa to 300 kPa with the uncertainty of ± 0.75 kPa.

To allow for affordable CFD simulations while providing relevant validation data, the ejector unit was designed to be axially symmetric, including the suction chamber. Furthermore, the modular character of the ejector unit enables the alteration of the unit geometry by changing its individual parts - nozzle, converging part, mixing tube, and diffuser. In this work, data were measured using several unit geometries. The one sketched in Figure A.2 with parts dimen-

sions from Table A.1 was the original configuration of the liquid-gas ejector unit used in [43] and it is referred to as the default geometry. Other used configurations resulted from the geometry optimization of the shape of the converging part and the diffuser. In optimization, only geometries with $d_N = 4.3$ mm and $d_M = 14$ mm were considered. The tested 'optimal' configurations, differing substantially in the total length of the ejector unit, were selected from the Pareto-optimal set.

In all cases, the converging part and diffuser were manufactured from polylactic acid (PLA) using an FDM 3D printer, 0.4 mm nozzle, and 0.2 mm layer height. The inner surface of the printed parts was polished with 1200 grit sandpaper and impregnated using an acrylic varnish. The manufacturing process produced airtight parts with surface smoothness comparable to that of stainless steel piping.

Appendix B. Mathematical model

A mathematical model of a single phase (water-water) ejector was prepared in the open-source C++ CFD library OpenFOAM (OpenFOAM Foundation version 8) [31]. The geometry of the physical device and the experimental setup are described in Appendix A. The corresponding CFD model was constructed with an emphasis on being computationally affordable and fully automated, including geometry generation and meshing. In the following, we present the flow governing equations considered, the applied boundary conditions and initial guess.

Appendix B.1. Governing equations

The flow in the water-water ejector was simulated to be pseudo-stationary, axisymmetric, isothermic and incompressible. Furthermore, water was assumed to be a Newtonian fluid, and the effects of turbulence were taken into account by Reynolds averaging. For the given case, the Reynolds-averaged Navier-Stokes

(RANS) equations take the form of

$$\begin{aligned}\nabla \cdot (\bar{\mathbf{u}} \otimes \bar{\mathbf{u}}) - \nabla \cdot (\bar{\boldsymbol{\tau}} + \boldsymbol{\tau}') &= -\nabla \bar{p} + \mathbf{g} \\ \nabla \cdot \bar{\mathbf{u}} &= 0,\end{aligned}\tag{B.1}$$

where $\bar{\mathbf{u}}$ and \bar{p} are the averaged velocity and kinematic pressure, respectively. Next, $\bar{\boldsymbol{\tau}} = \nu \nabla \bar{\mathbf{u}}$ is the averaged viscous stress tensor with ν being the fluid kinematic viscosity. The second stress tensor, $\boldsymbol{\tau}' = \mathbf{u}' \otimes \mathbf{u}'$, corresponds to the so-called Reynolds stress tensor where \mathbf{u}' is the instantaneous turbulence-driven velocity fluctuation. Finally, \mathbf{g} is the gravitational acceleration. Note that, hereafter, only the Reynolds-averaged variables will be taken into account and the bar over individual symbols will be omitted.

Due to the presence of the Reynolds stress term ($\nabla \cdot \boldsymbol{\tau}'$), the formulation (B.1) requires an additional closure model. Four two-equation eddy viscosity closure models were tested and chosen from, namely the k - ε model of Launder and Spalding [44] with rapid distortion theory (RDT) based compression term [45], realizable k - ε model by Shih et al. [46], k - ω model of Wilcox [47] and the Menter model k - ω shear stress transport (SST) model [48] in the formulation given by Hellsten [49].

Appendix B.2. Boundary conditions and initial guess

Both the system (B.1) and the selected turbulence closure model need to be completed with suitable boundary conditions. We divide the computational domain boundary into (i) *inlet* boundary representing the primary fluid inlet, (ii) *suction* boundary that corresponds to the secondary fluid inlet via the suction chamber, (iii) *outlet* boundary as the outlet from the ejector and (iv) *wall* boundary representing the system solid boundaries. The types of boundary conditions used for each section are given in Table B.1.

Most of the boundary conditions used are implemented by default in the OpenFOAM library [31]. The only exception is the boundary condition for the kinematic pressure at the suction boundary. An additional resistance term was added to reflect the hydraulic behavior of the experimental setup. In particular,

<i>inlet</i>		
\mathbf{u}	\tilde{p}	$k \mid \omega \mid \varepsilon$
fixed value	zero gradient	fixed value
<i>outlet</i>		
\mathbf{u}	\tilde{p}	$k \mid \omega \mid \varepsilon$
inlet-outlet	total pressure	inlet-outlet
<i>suction</i>		
\mathbf{u}	\tilde{p}	$k \mid \omega \mid \varepsilon$
inlet-outlet	total pressure with resistance	inlet-outlet
<i>wall</i>		
\mathbf{u}	\tilde{p}	$k \mid \omega \mid \varepsilon$
no-slip	zero gradient	wall functions

Table B.1: Applied boundary conditions.

the resistance is dependent on the secondary fluid flow rate (\dot{Q}_{suction}) and the final form of the boundary condition is

$$\tilde{p} = \tilde{p}^0 - \frac{1}{2} \|\mathbf{u}\|^2 + K_{\text{arm}} r_{\text{area}} \dot{Q}_{\text{suction}}^2, \quad (\text{B.2})$$

with \tilde{p}^0 being the total pressure, K_{arm} a piping resistance determined from the experimental data and r_{area} a ratio of the suction area available in experiment to the area of the *suction* boundary.

Finally, the problem specification was completed by prescribing a standard initial guess based on formulas by Russo and Basse [50].

Appendix B.3. Numerical settings

The flow governing equations (B.1) and the turbulence closure models tested were discretized within the C++ finite-volume library OpenFOAM [31]. The overall solution method was a segregated steady-state one. In particular, the pressure and velocity fields were solved by using the SIMPLE loop [51] with modifications described in Moukalled et al. [52], while the turbulence variables were updated at the end of each solver iteration. An emphasis was made on keeping the problem discretization as close to the second-order accuracy as possible. To do so, a second-order upwind scheme was used for discretization of the momentum equation convection term. For the convection of turbulence variables, a high-resolution scheme with the Minmod limiter by Roe [53] was utilized. For automatic simulation termination, the convergence criteria were set to 10^{-4} for all fields.

Appendix B.4. Mesh generation and mesh size independence study

The computational domain was based on a 2D axi-symmetric approximation of the ejector device. The computational mesh used is depicted in Figure B.1. The mesh was refined close to the walls, in order to keep the y^+ measure below 1. With the default ejector geometry (see Table A.1), the maximum non-orthogonality of the mesh was 25 degrees and the maximum skewness of the mesh was 0.6.

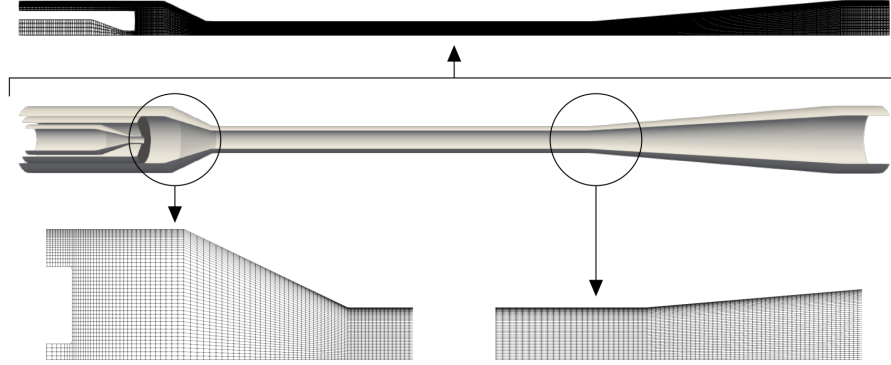


Figure B.1: Ejector geometry and qualitative view of the computational mesh. The overall mesh structure is shown in the top part of the figure, details of specific positions along the ejector are shown on the figure bottom.

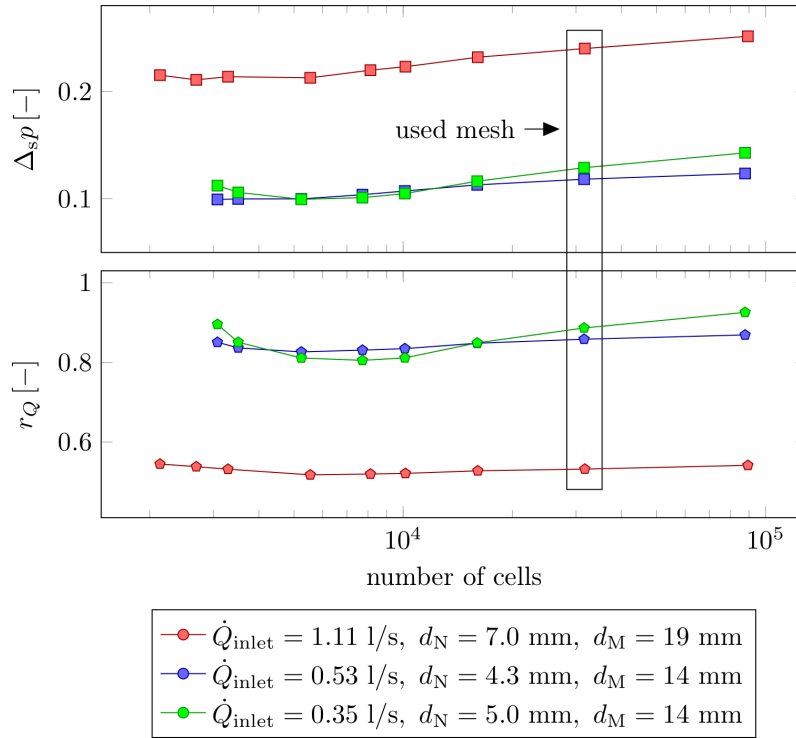


Figure B.2: Dependence of the scaled device pressure drop and secondary-to-primary flow rate ratio on the mesh resolution. Simulations were computed using the $k-\omega$ SST turbulence model.

To investigate the dependence of the results on the mesh resolution, two indicators were chosen. The first one was a scaled pressure drop of the device that was defined as

$$\Delta_{sp} := \frac{\bar{p}_{\text{outlet}} - \bar{p}_{\text{suction}}}{\bar{p}_{\text{inlet}} - \bar{p}_{\text{outlet}}}, \quad (\text{B.3})$$

where p stands for the kinematic pressure and the bars over variables denote surface-averages. The second indicator was a secondary-to-primary flow rate ratio computed as

$$r_Q = \dot{Q}_{\text{suction}} / \dot{Q}_{\text{inlet}} \quad (\text{B.4})$$

where \dot{Q} is the fluid flow rate. The same indicators were later used for model validation against experimental data. Note that the mesh size independence study was performed using the k - ω SST turbulence model.

Results of the mesh size independence study are shown in Figure B.2. Each data series corresponds to an ejector geometry with specified outer diameter of the nozzle (d_N) and diameter of the mixing tube (d_M). Each geometry was operated with different primary fluid flow rates (\dot{Q}_{inlet}) to cover the entire range of experimental data.

With increasing mesh resolution, there is a weak trend of increasing Δ_{sp} and r_Q . However, the indicators mostly level-out for meshes with more than 10^4 cells. Hence, the mesh having $\sim 3 \times 10^4$ cells (framed results in Figure B.2) was selected as the one providing the most suitable trade-off between the solution accuracy and computational cost.

Appendix B.5. Turbulence model selection

Experimental data measured on a geometry with $d_N = 5.0$ mm and $d_M = 14$ mm were used to test different turbulence models, namely the k - ω SST, k - ω , k - ε and realizable k - ε model. The results are presented in Figure B.3.

Note that in Figure B.3 and later in Figure B.4, there are two or more distinct values for each \dot{Q}_{inlet} . This is due to the fact that all measurements were repeated more times, each time with different total pressure before suction ($\bar{p}_{\text{suction}}^0$). In simulation, $\bar{p}_{\text{suction}}^0$ is an input parameter and was set accordingly

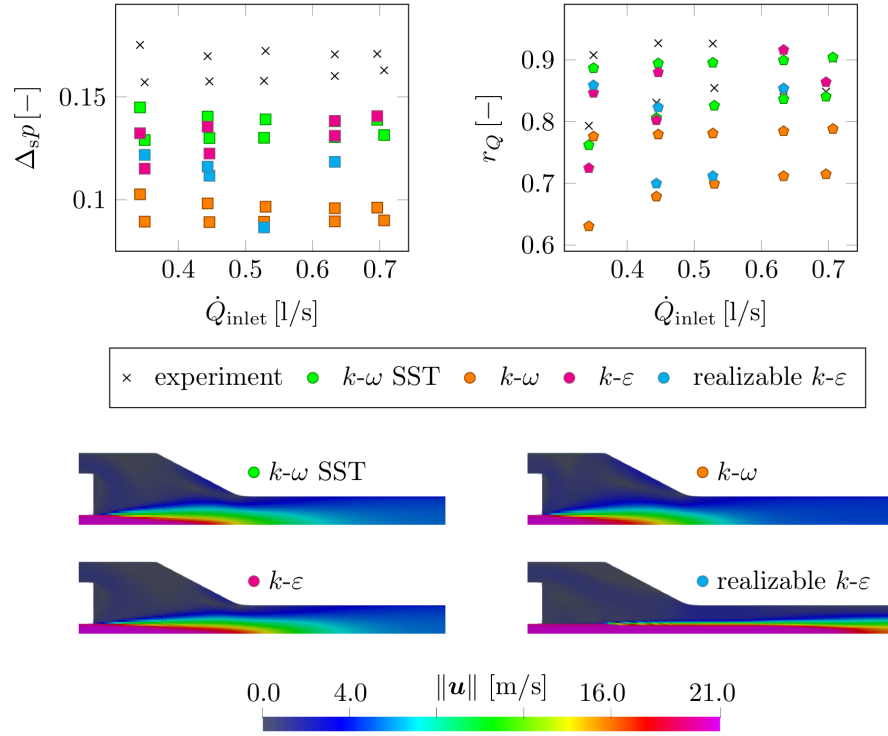


Figure B.3: Comparison of experimental and simulation data computed with different turbulence models for the ejector geometry with $d_N = 5.0$ mm and $d_M = 14$ mm. Velocity fields predicted by each turbulence model are given at the figure bottom.

to the experimental value. Hence, these series are not differentiated in the aforementioned figures.

Based on comparison with experimental data, the most suitable models seemed to be $k-\omega$ SST and $k-\varepsilon$. However, simulations that run with the $k-\varepsilon$ model had significant problems with stability and convergence speed. Therefore, the $k-\omega$ SST model was chosen.

Appendix B.6. Model validation

The prepared CFD model was validated against specifically measured experimental data. The data were measured on three different ejector geometries (specified by d_N and d_M) and with varying primary fluid flow rates (\dot{Q}_{inlet}). The simulation and experimental data were compared focusing on the scaled pressure drop of the device (Δ_{sp}) and secondary-to-primary flow rate ratio (r_Q), defined in Section [Appendix B.4](#).

The comparison of the experimental and simulation data is presented in [Figure B.4](#) and [Figure B.5](#). For a given ejector geometry, the CFD model slightly over- or under-predicts the performance indicators. Nonetheless, the error is always within the range of ± 20 % of its measured value, as shown in [Figure B.5](#). Although the agreement in the experimental and simulation data is not perfect, the simulations were able to catch the trends of indicator changes with respect to flow rate and device geometry, see [Figure B.4](#). As this simulation capability is essential for geometry optimization, the agreement with the experimental data was deemed acceptable for further use in the optimization framework.

Appendix C. CFDNetAdapt settings

The setting of CFDNetAdapt hyperparameters used for the ZDT functions is listed in [Table C.1](#) and for the real-life application in [Table C.2](#). In both cases, the process of tweaking the algorithm hyperparameters was similar.

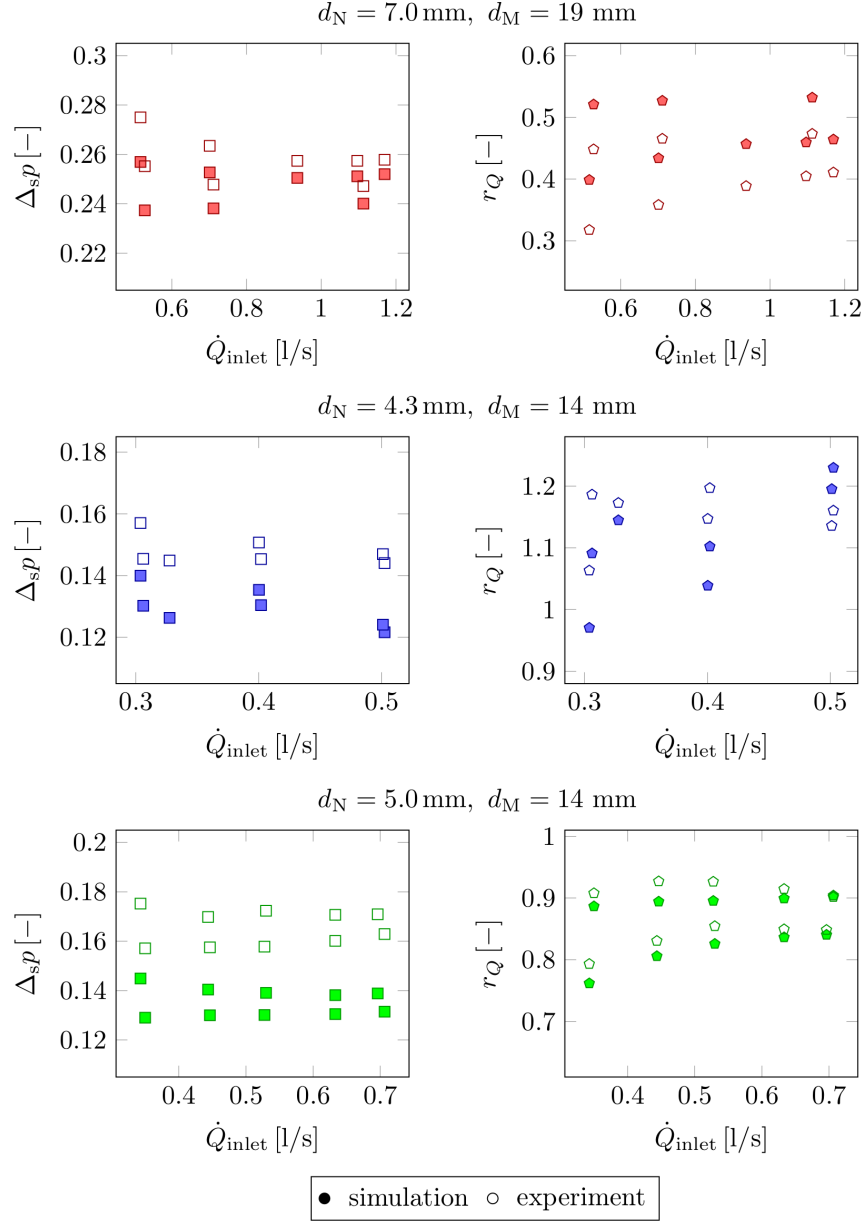


Figure B.4: Comparison of simulation and experimental data, namely the scaled device pressure drop (Δ_{sp}) and secondary-to-primary flow rate ratio (r_Q) for three different ejector geometries. Simulation data were computed using the $k-\omega$ SST turbulence model.

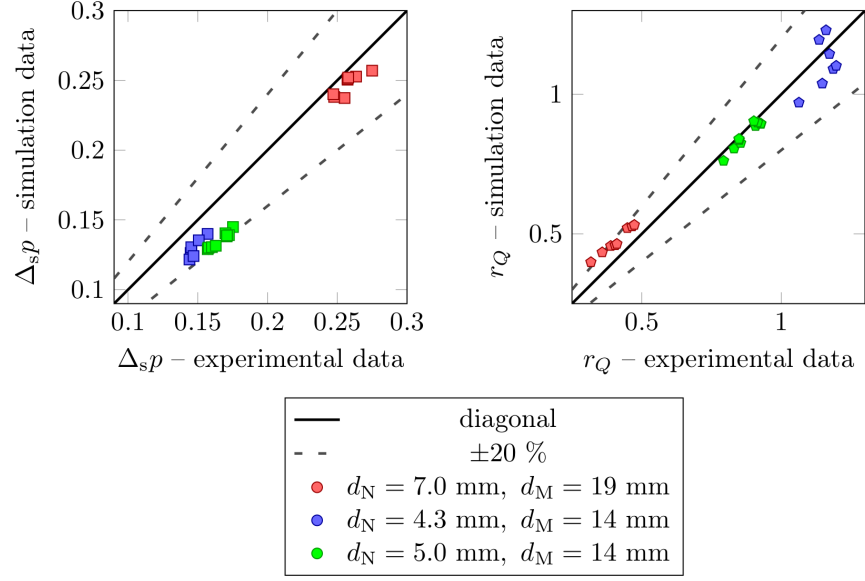


Figure B.5: Parity plot showing all experimental and simulation data presented in Figure B.4 together.

hyperpar.	value	hyperpar.	value	hyperpar.	value
n_{hlrs}	3	n_{min}	2	n_{gen}	250
n_{dnn}	4	n_{max}	20	n_{ver}	16
$\{\bar{n}_1, \bar{n}_2, \bar{n}_3\}$	$\{11, 11, 11\}$	n_{smp}	1,000	k_{max}	25
r_n	4	n_{pop}	100	ϵ	10^{-4}

Table C.1: Values of CFDNNAdapt parameters used for the ZDT functions.

hyperpar.	value	hyperpar.	value	hyperpar.	value
n_{hlrs}	3	n_{min}	2	n_{gen}	90
n_{dnn}	10	n_{max}	20	n_{ver}	8
$\{\bar{n}_1, \bar{n}_2, \bar{n}_3\}$	$\{11, 11, 11\}$	n_{smp}	600	k_{max}	12
r_n	4	n_{pop}	500	ϵ	0.05

Table C.2: Values of CFDNNAdapt parameters used for the real-life application.

Several parameters were tuned by manually testing a few MLPs with different layer sizes and observing their behavior in optimization. In this way, the hyperparameters n_{hlrs} , $\{\bar{n}_1, \bar{n}_2, \bar{n}_3\}$, r_n , n_{min} , n_{max} , n_{pop} and n_{gen} were set.

Then, we ran CFDNNetAdapt without the verification step to tune the hyperparameters n_{dnn} , n_{smp} , Δ_{smp} and Δr_n . The results of the last adjustment step were used to perform a manual verification to set the hyperparameters n_{ver} and ϵ . Lastly, k_{max} was set to be three times the expected number of steps, since n_{smp} is limited by the number of available CFD data points.

Appendix D. Additional data from validation of optimization results

The comparison of all available experimental data with the data from the corresponding CFD models is shown in Figures D.1 and D.2. The comparison is based on two indicators presented in Appendix B.6, namely the scaled device pressure drop (Δ_{sp}) defined in (B.3) and the secondary-to-primary flow rate ratio (r_Q) defined in (B.4).

The data show trends similar to the data presented in model validation in Appendix B.6. For a given design, the CFD model tends to over- or under-predict the experimental data, but the error stays in the bounds of ± 20 % of the measured value.

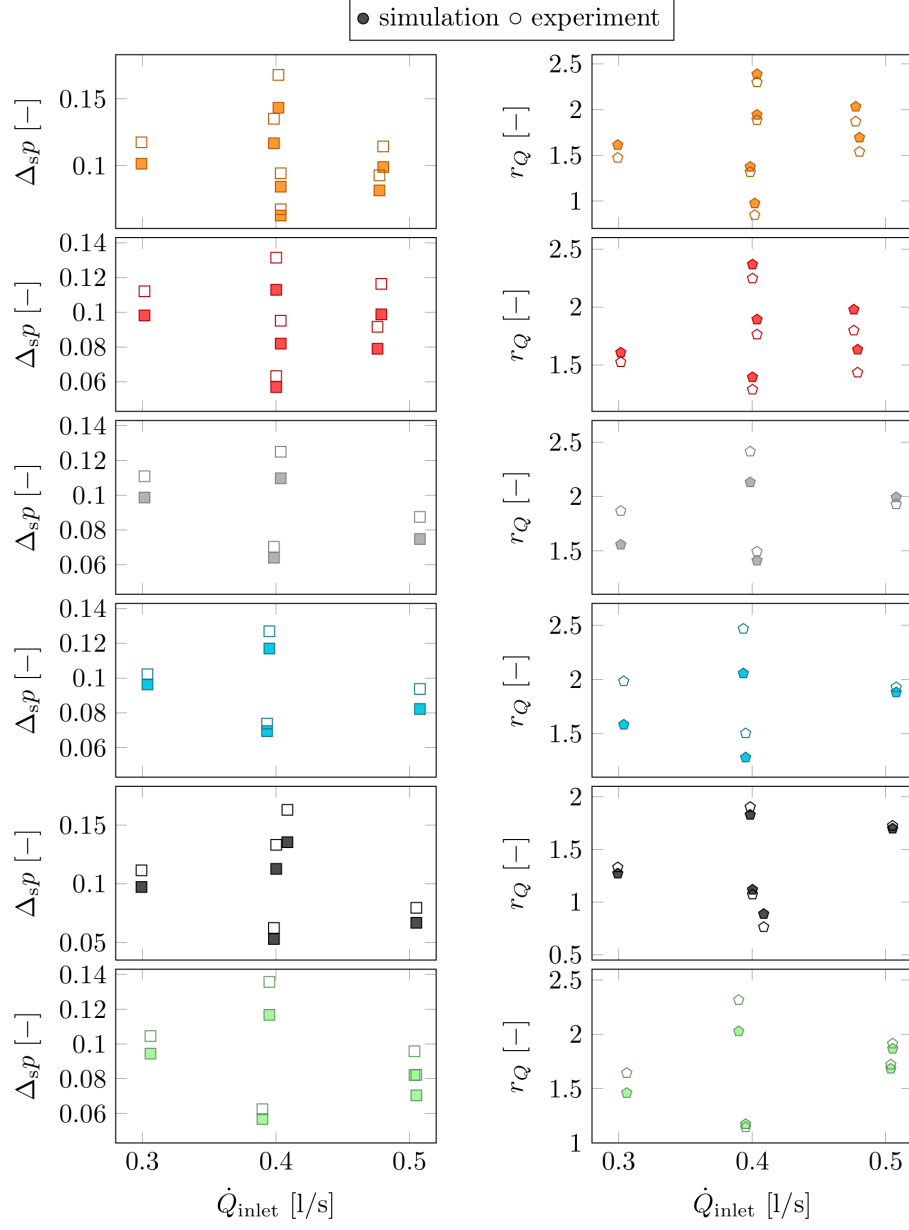


Figure D.1: Comparison of simulation and experimental data, namely the scaled pressure drop (Δ_{sp}) and the secondary-to-primary flow rate ratio (r_Q) are depicted for different primary fluid flow rates \dot{Q}_{inlet} . Colors correspond to ejector designs displayed in Figure 8.

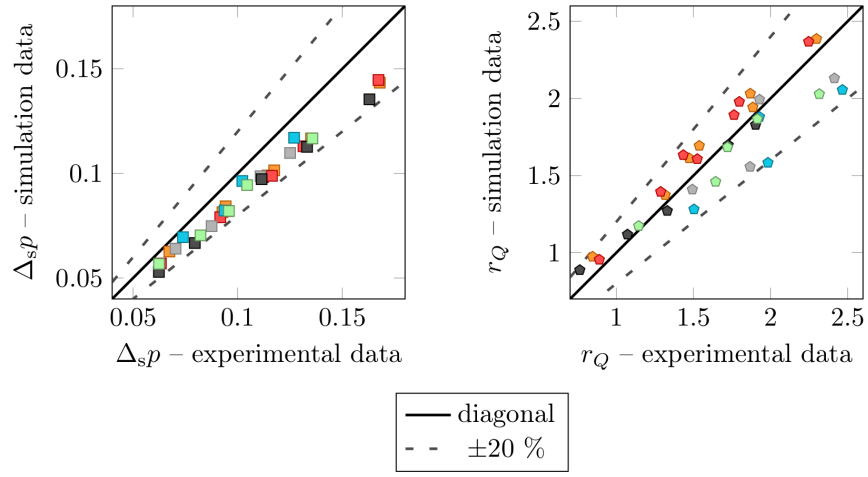


Figure D.2: Parity plot showing all experimental and simulation data presented in Figure D.1 together. Colors correspond to designs displayed in Figure 8.